

Development of an Electromagnetic Coil Array for a Small-Scale Rotating Magnetic Field Plasma Thruster

A project presented to
The Faculty of the Department of Aerospace Engineering
San José State University

in partial fulfillment of the requirements for the degree
Master of Science in Aerospace Engineering

by

Andrew F. Strauss

May 2023

approved by

Ali Guarneros Luna
Faculty Advisor

© 2023
Andrew F. Strauss
ALL RIGHTS RESERVED

ABSTRACT

Development of an Electromagnetic Coil Array for a Small-Scale Rotating Magnetic Field Plasma Thruster

Andrew F. Strauss

Plasma thrusters are desired for use in space propulsion because they have the high specific impulse ranges typical of electric propulsion while still maintaining relatively high thrust. Electrodeless plasma thrusters generate plasma without any electrodes in direct contact with it, which increases system longevity. Rotating magnetic field thrusters are electrodeless thrusters that generate and accelerate plasma with a rotating magnetic field. The goal of this project was to develop an electromagnetic coil array for use in a small-scale rotating magnetic field electrodeless plasma thruster. CFD simulations of various electromagnetic coil configurations were performed to identify the configuration most suitable for thrust production. After a suitable configuration was selected, a prototype coil array was constructed based on that configuration. The vacuum magnetic field of the prototype coil array was measured, and these measurements were compared to those obtained from the simulation environment. It was concluded that the simulation environment had been suitably validated for simulating vacuum magnetic fields. Suggestions were made for future work that uses the results of this project to further develop the coil array.

Acknowledgements

I would like to thank my advisor, Professor Ali Guarneros Luna, for her guidance over the course of this project, and for the encouragement she gave me in picking a topic that fit my fields of interest. I would also like to thank my family for the support and encouragement of my education that they have given me over the course of it.

Table of Contents

1	Introduction.....	1
1.1	Motivation	1
1.2	Literature Review.....	1
1.3	Project Proposal.....	6
1.3.1	Project Goals.....	6
1.3.2	Requirements	6
1.3.3	Process	7
1.4	Methodology	7
1.4.1	Simulation.....	7
1.4.2	Prototype.....	8
2	Simulation Environment.....	10
2.1	Introduction	10
2.2	Software Selection.....	10
2.3	Software Validation.....	10
2.3.1	Goals	10
2.3.2	Geometry.....	10
2.3.3	Mesh.....	11
2.3.4	Physics Modeling.....	12
2.3.5	Results.....	13
3	Thruster Simulations.....	16
3.1	Geometry	16
3.1.1	Thruster Body	16
3.1.2	RMF Coils.....	17
3.1.3	Axial Coil Configurations.....	17
3.2	Mesh.....	20
3.3	Physics Modeling	22
3.4	Results and Discussion.....	22
3.4.1	Electromagnetic Characteristics.....	22
3.4.2	Thruster Performance.....	23
3.4.3	Electrical Power Requirements.....	24
3.4.4	Configuration Selection	26
4	Prototype Design – RMF Generation	28

4.1	Introduction	28
4.2	Signal Generation.....	28
4.3	RMF Coil Design	31
4.4	Test Results and Discussion.....	36
4.4.1	Signal Generation Testing.....	36
4.4.2	Coil Reactance Testing	39
5	Prototype Design – Axial Coil and Power Systems.....	41
5.1	Introduction	41
5.2	Axial Coil Design.....	41
5.3	RMF Amplifier Design	44
5.4	System Power Input Measurement.....	48
6	Magnetic Field Measurement and Simulation Environment Validation	50
6.1	Introduction	50
6.2	Magnetic Field Measurement.....	50
6.3	Simulation Environment Validation.....	52
6.4	Results and Discussion.....	54
6.4.1	Rotating Magnetic Field Comparison.....	54
6.4.2	Axial Magnetic Field Comparison.....	57
7	Conclusion and Suggestions for Future Work	58
8	References.....	59
	Appendix A – Derivation of Reactance Testing Equation.....	61

List of Tables

Table 1.1 – Commercial EPT performance parameters [17].	4
Table 1.2 – Project requirements.	7
Table 3.1 – Net Lorentz force in the x-direction.	23
Table 3.2 – Nondimensional thruster performance parameters.	24
Table 3.3 – Thruster electrical performance parameters.	25
Table 3.4 – Input power required for the axial coils.	26
Table 3.5 – Axial coil x-direction Lorentz force and input power.	27
Table 5.1 – Amplifier circuit output measurements.	47
Table 5.2 – Calculated load reactance values.	47
Table 5.3 – Amplifier circuit output measurements for coil-only load.	48
Table 5.4 – Power supply channel measurements of prototype electrical systems.	48

List of Figures

Figure 1.1 – Example RMF thruster configuration [2].	3
Figure 1.2 – Diagram of the NTU experiment plasma generation configuration [3].	6
Figure 1.3 – Prototype system block diagram.	9
Figure 2.1 – Geometry used in the validation study simulations.	11
Figure 2.2 – Cross-section of the plasma vessel mesh.	12
Figure 2.3 – Component of current density tangent to the y-z plane.	13
Figure 2.4 – Cross-section of the temperature profile in the plasma vessel.	15
Figure 3.1 – Thruster body geometry.	16
Figure 3.2 – RMF coil array geometry.	17
Figure 3.3 – RMF Only thruster configuration.	18
Figure 3.4 – Single Coil thruster configuration.	18
Figure 3.5 – Varying Size thruster configuration.	19
Figure 3.6 – Varying Current thruster configuration.	19
Figure 3.7 – Mini-ELF thruster configuration.	20
Figure 3.8 – Cross section of the thruster mesh in the x-y plane.	21
Figure 3.9 – Cross section of the thruster mesh in the y-z plane.	21
Figure 3.10 – Component of current density tangent to the y-z plane.	23
Figure 3.11 – RMF coil equivalent circuit diagram.	25
Figure 4.1 – Signal generator circuit from the XR2206 datasheet [24].	29
Figure 4.2 – High pass filter and phase splitter circuit diagram.	30
Figure 4.3 – The assembled signal generator circuit.	31
Figure 4.4 – Schematic diagram of the RMF coil array scaffold tube.	32
Figure 4.5 – Top view of the RMF coil array.	33
Figure 4.6 – Side view of the RMF coil array.	34
Figure 4.7 – Perspective view of the RMF coil array.	35
Figure 4.8 – Reactance testing circuit diagram.	36
Figure 4.9 – Oscilloscope measurement of both phase splitter outputs.	37
Figure 4.10 – Oscilloscope measurement of output 1 of the phase splitter.	38
Figure 4.11 – Oscilloscope measurement of output 2 of the phase splitter.	38
Figure 5.1 – Schematic diagram of the axial coil scaffold.	42
Figure 5.2 – 3D printed axial coil scaffold.	43
Figure 5.3 – Axial coil winding.	44
Figure 5.4 – Amplifier circuit diagram from the LT1210 datasheet [26].	45
Figure 5.5 – Assembled RMF amplifier circuit.	46
Figure 6.1 – Fully assembled coil array.	51
Figure 6.2 – Hall effect sensor magnetic field-voltage response curve [27].	52
Figure 6.3 – Simulated geometry of the coil array prototype.	53
Figure 6.4 – Cross section of the prototype simulation mesh in the x-y plane.	53
Figure 6.5 – Measured Hall effect sensor output voltage for the RMF test.	54
Figure 6.6 – Measured magnetic field strength of the rotating magnetic field y-component.	55
Figure 6.7 – Simulated magnetic field strength of the rotating magnetic field y-component.	56
Figure 6.8 – Comparison between measured and simulated RMF strength.	57

Symbol	Definition	Units
A	Magnetic vector potential	V·s/m
A	Amplitude	-----
B	Magnetic flux density	T
C	Capacitance	F
E	Electric field	N/C
I, i	Electric current	A
J	Current density	A/m ²
j	Imaginary unit (circuit theory applications)	-----
L	Inductance	H
n	Particle number density	m ⁻³
q	Electric charge	C
R	Electrical resistance	Ω
t	Time	s
V, v	Voltage	V
X	Reactance	Ω
Z	Complex impedance	Ω
Greek Symbols		
η	Resistivity	Ω·m
θ	Phase angle	rad
μ	Magnetic permeability	H/m
ω	Angular frequency	rad/s
Subscripts		
() _e	Electron property	-----
() ₀	Vacuum property	-----
Acronyms		
AC	Alternating Current	-----
CFD	Computational Fluid Dynamics	-----
DC	Direct Current	-----
ELF	Electrodeless Lorentz Force	-----
EPT	Electrodeless Plasma Thruster	-----
FFF	Fused Filament Fabrication	-----
FRC	Field Reversed Configuration	-----

GER	Gradually Expanded Rotamak	-----
ICRH	Ion Cyclotron Resonance Heating	-----
MHD	Magnetohydrodynamics	-----
NASA	National Aeronautics and Space Administration	-----
NTU	Nanyang Technological University	-----
PLA	Polylactic Acid	-----
RF	Radio Frequency	-----
RMF	Rotating Magnetic Field	-----
SJSU	San Jose State University	-----
VASIMR	Variable Specific Impulse Magnetoplasma Rocket	-----

1 Introduction

1.1 Motivation

Plasma thrusters are desired for use in space propulsion because they have the high specific impulse ranges typical of electric propulsion while still maintaining relatively high thrust. Typical plasma propulsion schemes generate plasma with electrodes in direct contact with the working fluid. However, it is desirable to generate plasma without these electrodes. A plasma propulsion scheme where there are no electrodes in contact with the plasma prevents electrode erosion, which is a major limiting factor in the longevity of other forms of plasma propulsion [1]. Electrodeless plasma propulsion schemes typically use externally applied electromagnetic fields to generate and accelerate plasma.

There are many different electromagnetic field configurations being investigated for use in electrodeless plasma thrusters [2]. Many of these configurations have high power requirements, which would likely limit their use to large-scale spacecraft. Additionally, high power requirements likely increase the time it will take for these propulsion schemes to be viable for actual spaceflight. High power systems tend to have higher mass, and increasing mass of a spacecraft increases the difficulty and cost of launching it. A low power plasma thruster concept would then be desirable for quicker implementation in actual spaceflight.

Several electromagnetic field configurations have been investigated for use at smaller-scale power levels. One is notable for not requiring a pre-ionization phase, which reduces the overall system complexity. The researchers investigating this configuration suggested a use case of small satellite propulsion [3], but it could likely have applications for small-scale deep space spacecraft as well. While the experiment on this configuration was successful in generating plasma, it was not configured for thrust production. The researchers who performed the experiment recommended that more work should be performed to develop this small-scale rotating magnetic field plasma generation concept to produce thrust [3].

1.2 Literature Review

There are many electrodeless plasma thruster concepts under investigation at various stages of development. One of the more widespread concepts is the helicon thruster. Helicon thrusters generate plasma using a type of electromagnetic wave called a helicon. Helicon waves are often used for plasma generation in thruster applications, but they have limited utility for plasma acceleration. The acceleration methods that a helicon source has access to are pressure against the back wall of the thruster, and a diverging magnetic field that acts like a nozzle for the plasma flow. In general, a diverging magnetic field that is used as a diverging nozzle for plasma flow is called a magnetic nozzle [2].

Because of the limited acceleration methods, helicon plasma sources are often combined with a separate electromagnetic antenna configuration to accelerate the plasma. An example of a helicon source combined with another acceleration method is the VASIMR propulsion concept. VASIMR uses a helicon source to generate plasma, but then adds energy to the flow with ion cyclotron resonance heating. ICRH involves applying an electromagnetic field with the same

frequency as the ion cyclotron frequency of the plasma. This causes resonance and greatly increases the temperature of the plasma. VASIMR also uses a magnetic nozzle to expand and further accelerate the flow [4]. The VASIMR concept was originally developed at the NASA Johnson Space Center in 1980, and research on it has been continued in the form of laboratory experiments and theoretical studies [5]. At present, the VASIMR concept is being developed by the private company Ad Astra Rocket Company, and it is at the stage of laboratory prototype testing. The most recent tests have established a high-power performance benchmark for the current VASIMR system, and demonstrated the continuous operation endurance of current prototypes [6].

A variant of the helicon thruster concept is the helicon double layer configuration. This configuration is based on the ability of a helicon plasma source to generate an electric double layer [7]. An electric double layer is a region of plasma where two adjacent layers of opposing charge form. The buildup of opposing charges causes a double layer to have a large electric potential gradient. In the context of a thruster, the potential gradient of a double layer can be used to accelerate plasma to supersonic speeds, which can significantly increase the thrust produced by the flow [8]. The helicon double layer thruster concept has been primarily investigated by a team at Australian National University. Development of the helicon double layer thruster to date has mainly consisted of laboratory tests and simulations [9,10]. A news article from 2009 suggests that an in-space flight test of a helicon double layer thruster was planned [11], but it is unclear if this mission was ever carried out.

Another EPT concept under development is the rotating magnetic field configuration. Rotating magnetic field thrusters generate plasma using a rotating magnetic field. In an RMF thruster, the rotating magnetic field is generated using two sets of orthogonal coils that carry sinusoidal currents with a phase difference of 90 degrees. If the rotating magnetic field is configured correctly, it will cause the electrons in the working fluid to move circularly with the same angular velocity and direction as the magnetic field. The plasma is then generated in a closed topology called a field reversed configuration plasmoid. The circular motion of the electrons results in large currents in the azimuthal direction. The presence of an additional magnetic field in the radial direction would then cause the plasmoid to undergo a Lorentz force in the axial direction. This is the main method of plasma acceleration, and therefore thrust production, in an RMF thruster. The radial magnetic field component is typically introduced by using another electromagnetic coil array that produces an axial magnetic field gradient [2,12].

An example of a rotating magnetic field coil array is shown in Figure 1.1. The orthogonal coils parallel to the flow axis are the core components of the RMF generation. Any additional coils present are typically used to generate the axial magnetic field gradient, and the configuration used for this varies between thruster concepts.

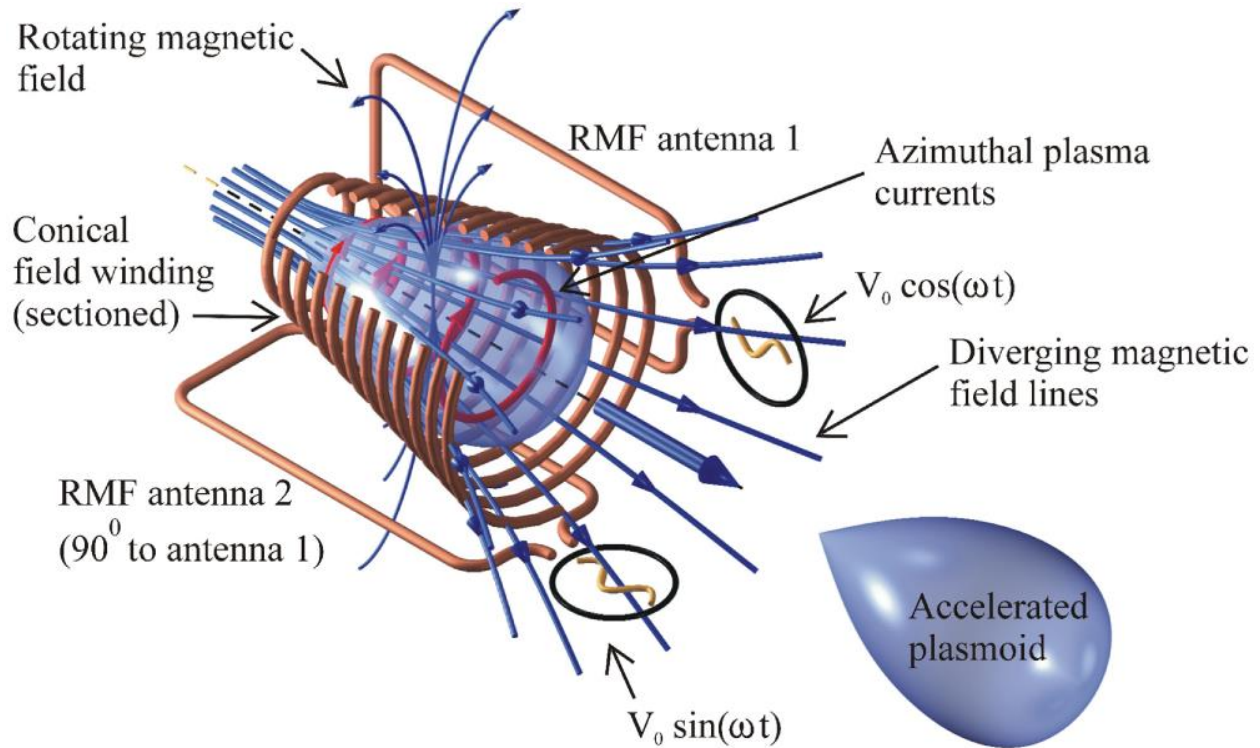


Figure 1.1 – Example RMF thruster configuration [2].

One thruster concept that uses a rotating magnetic field configuration is the electrodeless Lorentz force thruster. The ELF thruster uses the previously described coil configuration to generate the FRC plasmoid, and a conical solenoid to generate the axial magnetic field gradient. The containment region for the FRC is also conical. In addition to these components, the ELF thruster also includes a pre-ionization phase to ionize the working fluid into a plasma before it is introduced into the rotating magnetic field. The ELF concept has been developed to the point of laboratory testing. These tests have successfully demonstrated FRC generation, FRC ejection, and thrust production capabilities of the ELF concept [12].

Another electrodeless plasma thruster concept uses both a helicon and an RMF configuration. In this configuration, the helicon wave antenna is used to ionize the propellant gas flow into a plasma. After the plasma column is formed, it enters the rotating magnetic field, which forms an FRC plasmoid. Additionally, a combination of permanent and electromagnets are used to generate an axial magnetic field. This axial magnetic field is used to assist in generating the plasma column, and to provide the gradient necessary to accelerate the plasmoid. This hybrid concept was developed by a research team at the Tokyo University of Agriculture and Technology [13]. To date, this concept has been developed to the level of laboratory experiments. Recent experiments by the Tokyo University research team have involved validating the predicted effects of the RMF on the plasma [14].

One study suggests that the efficiency of plasma thrusters tends to increase as input power increases [2]. It is likely for this reason that many electrodeless plasma thruster concepts are being developed for high power use in large-scale spacecraft. However, small-scale plasma thruster concepts are being developed as well. A study from the Tokyo University of Agriculture and Technology investigated plasma generation for EPT systems at very small scales. The study investigated plasma discharge tube sizes ranging from 3 mm diameter at the largest to 0.5 mm diameter at the smallest. The plasma generation was accomplished with RF antennas and supported with electromagnets. The study was successful in identifying configurations for plasma generation at the scales tested. However, no methods of thrust production were tested at these scales [15].

There are a few small satellite propulsion systems currently in production that use electrodeless plasma thrusters. One of these is the Maxwell propulsion system family developed by the company Phase Four. The thruster used in the Maxwell system uses an electromagnetic RF antenna to generate the plasma, and a permanent magnet to accelerate it [16]. The specific configuration of this antenna is proprietary [16], and information about it is not publicly available. These systems produce thrust in the millinewton range, and operate on an input power of less than 500 W. Two small satellites using Maxwell propulsion systems were launched as part of the SpaceX Transporter-1 mission in 2021 [17].

Another commercial electrodeless plasma propulsion system for small satellites is the REGULUS propulsion system family developed by the company T4i. The thruster uses a type of helicon configuration, but no specific details of this configuration have been made publicly available [18]. The REGULUS systems produce thrust on the order of hundreds of micronewtons, and operate on an input power of 50 W. A REGULUS propulsion system was included in the UniSat-7 technology demonstration mission in 2021 [17].

Performance parameters of the Maxwell and REGULUS systems are shown in Table 1.1. These values can be used as a comparison metric for the plasma thruster system developed in this project. However, since the exact plasma generation configurations of these commercial propulsion systems are unknown, there are limits to how meaningful this comparison can be. It is notable that these commercial propulsion systems have low specific impulse values; electric propulsion systems typically have specific impulse values on the order of thousands of seconds.

Table 1.1 – Commercial EPT performance parameters [17].

Propulsion System	Thrust	Specific Impulse	Input Power	Thrust to Power Ratio
Maxwell	5.5-6 mN	400-800 s	450 W	12.2-13.3 mN/kW
REGULUS	0.55 mN	550 s	50 W	11 mN/kW

The small-scale electrodeless plasma thruster concept that will be used in this project comes from Nanyang Technological University in Singapore. This concept is called the gradually expanded Rotamak configuration [19]. The GER concept uses a rotating magnetic field configuration where the FRC plasmoid is generated in a spherical containment region. The GER concept has a relatively small size and power requirement, using a plasma containment region of 28 cm and a power input of 800 W at maximum. Notably, this makes it larger than the two commercially available small satellite EPT propulsion systems. However, a major notable quality of this concept is that it does not require a pre-ionization phase; the RMF coils are used to both ionize the plasma and generate the FRC plasmoid. This reduces system complexity by eliminating the need for an additional electromagnetic field generation apparatus [3].

The idea for the GER plasma thruster was developed from a nuclear fusion reactor concept called a Rotamak. The Rotamak was developed at Flinders University in Australia as a containment device for toroidal plasmas. The Rotamak concept consists of a spherical containment region holding a plasma generated by a rotating magnetic field. The rotating magnetic field of a Rotamak is generated using the same type of orthogonal electromagnetic coil configuration used for an RMF thruster. Additionally, an additional set of orthogonal electromagnetic coils (aligned in the axial direction) is used to confine the generated plasma [20]. In the original fusion reactor concept, this third set of coils is symmetric to keep the plasma in equilibrium. In the GER thruster concept, these axial coils could be made asymmetric to generate the axial magnetic field gradient typically used for thrust production.

In the GER plasma thruster concept and the fusion research that preceded it, the plasma physics are modeled using a magnetohydrodynamics model with added assumptions. The assumptions used are as follows:

- The plasma is treated as two separate species: ions and electrons
- The ions are considered to be immobile
- The electrons are considered to be a massless fluid and their inertia is neglected

The assumption of fixed ions is valid when the frequency of the rotating magnetic field is greater than the ion cyclotron frequency and less than the electron cyclotron frequency. These assumptions significantly simplify the magnetohydrodynamics equations that describe the plasma formation and flow [21]. This model has been used to mathematically describe the penetration of the RMF into the plasma, the formation of the azimuthal currents, and the formation of the FRC plasmoid [3,21].

Development of the GER configuration has reached the level of laboratory experiments. The experiment performed at NTU was successful in using the GER configuration to generate plasma. However, this experiment was not configured to accelerate the plasma and produce thrust. The axial coils used the symmetric configuration of the original Rotamak concept, so there was no gradient in the applied axial magnetic field. Since the plasma generation proof of concept was successful, the NTU research team suggested that more research should be done to develop a functional thruster from the GER concept [3]. Such research would likely include developing methods of thrust production based on the Rotamak configuration.

1.3 Project Proposal

1.3.1 Project Goals

The proposed project is to develop an electromagnetic antenna configuration for use in a small-scale RMF plasma thruster. This will be accomplished by modifying the GER rotating magnetic field antenna configuration used in the NTU experiment. The project will consist of two stages. The first stage of the project will be to perform numerical simulations to identify potential thrust producing antenna configurations. After several thrust producing configurations have been identified, the second stage of the project will be to construct a prototype of the most promising of the identified antenna configurations.

The GER configuration used in the NTU proof of concept experiment will be used as the basis for this project. This configuration was chosen due to its small size, low input power, and reduced system complexity compared to other electrodeless plasma thruster concepts. The GER configuration consists of a spherical plasma containment region and three orthogonal sets of electromagnetic coils. This configuration will then be modified to identify avenues of thrust production. Parameters to be modified will include the physical geometry of the configuration (such as the plasma containment region) and the topology of the applied electromagnetic fields. A diagram of the configuration used in the NTU experiment is shown in Figure 1.2.

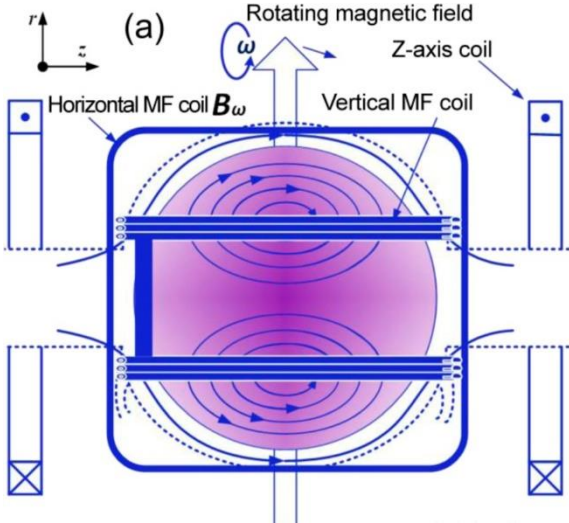


Figure 1.2 – Diagram of the NTU experiment plasma generation configuration [3].

1.3.2 Requirements

Since this propulsion scheme is intended for small-scale applications, the main requirements for this project concern the size and input power of the thruster. The requirement targets are shown in Table 1.2.

Table 1.2 – Project requirements.

Req. Number	Description	Parameter	Target
1	The diameter of the coil array shall not exceed 28 cm	Coil array diameter	28 cm
2	The power input to the coil array system shall not exceed 1 kW	Input power	1 kW

The targets for both requirements were chosen based on the NTU experiment, which used a plasma containment vessel diameter of 28 cm and a maximum input power of 800 W [3]. These parameters were set as upper bounds for this project to ensure that the developed thruster can be considered small-scale.

Since a goal of the project is to develop a new configuration for thrust production, it is unknown what range the thruster performance parameters will lie in. Because of this, it is not feasible to specify requirement targets for any thruster performance parameters. Instead, performance parameters will be considered figures of merit for the designs in the simulation phase. Performance parameters used as figures of merit will include thrust, specific impulse, input power, and the ratio of thrust to input power.

1.3.3 Process

The first step of the project will be to simulate the NTU experiment configuration to ensure that the chosen simulation method produces realistic results. Then, several different rotating magnetic field antenna configurations will be chosen as candidates for thrust production. The plasma generation and acceleration of these configurations will then be simulated in order to identify configurations that generate thrust. Identified thrust-producing configurations will then be evaluated based on performance parameters such as net thrust produced, specific impulse, and the ratio of thrust to electric power input.

After the most viable configuration has been identified from the simulations, a prototype of that configuration will be constructed. This will consist of constructing the array of electromagnetic coils and RF generators identified in the simulated configuration. After construction, the prototype will be tested to verify whether the electromagnetic field it generates in a vacuum (i.e. in the absence of plasma formation) matches what is simulated.

1.4 Methodology

1.4.1 Simulation

The models used for the simulation phase will be chosen based on the models typically used to describe the formation of plasma in a rotating magnetic field. As described in Section 1.2, the model typically used for this application is a simplified MHD model with assumptions of fixed ions and massless electrons. These assumptions simplify the MHD equations into the equations shown in Eqs. (1.1)-(1.3) [21]. These are the governing equations of this model.

$$\frac{\partial \mathbf{A}}{\partial t} = -\eta \mathbf{J} - \frac{1}{q_e n} \mathbf{J} \times \mathbf{B} \quad (1.1)$$

$$\mathbf{B} = \nabla \times \mathbf{A} \quad (1.2)$$

$$\mathbf{J} = \frac{1}{\mu_0} \nabla \times \mathbf{B} \quad (1.3)$$

This model has historically been used in specialized simulation codes for rotating magnetic field applications. However, this project will use commercial CFD software with MHD capabilities to carry out the simulation phase. Modern CFD software that has plasma simulation capabilities tends to use more general MHD models to suit a variety of cases. A less restricted MHD model requires governing equations for the fluid behavior of a plasma (e.g. momentum and energy equations) in addition to the equations for its electromagnetic behavior.

In addition to the restricted model for RMF applications described above, a more generalized MHD version of this model with fewer assumptions has also been developed [22]. This extended model will be consulted in order to choose appropriate parameters for the general MHD model used in the simulation software used in this project.

The initial simulations of the proof-of-concept case will be performed with axisymmetric and 2D geometry configurations. Simulations of thrust producing configurations will be performed with an axisymmetric geometry configuration. If the axisymmetric assumption proves insufficient to capture the necessary physics, full 3D simulations will be performed. All simulations will be performed using a finite volume computational method.

1.4.2 Prototype

The prototype will consist of two subsystems: the RMF generation subsystem and the axial magnetic field generation subsystem. The RMF generation subsystem will consist of an AC signal generator, a 90-degree signal splitter, two power amplifiers, impedance matching networks, and the two orthogonal sets of RMF coils. The structure of this subsystem is based on the system used in the NTU experiment [3] and a different RMF plasma experiment from Princeton [23]. The axial magnetic field generation subsystem will consist of a DC power supply and the axial magnetic field coils. The exact configuration of the axial coils used in the prototype will be determined based on the results of the simulation phase.

The prototype will be tested by measuring its generated magnetic field using Hall effect sensors. These sensors will be placed at predetermined locations within the prototype. The sensor readings at these locations will be compared to magnetic field strength data from the corresponding locations in the simulation. The full test apparatus system consists of the Hall effect sensors, signal amplifiers, and an oscilloscope.

Testing of the prototype will occur in a vacuum environment. This will be accomplished using one of the vacuum chambers available in the space systems lab at SJSU.

A block diagram of the entire prototype system is shown in Figure 1.3. This diagram depicts the RMF generation subsystem, the axial magnetic field generation subsystem, and the test apparatus system.

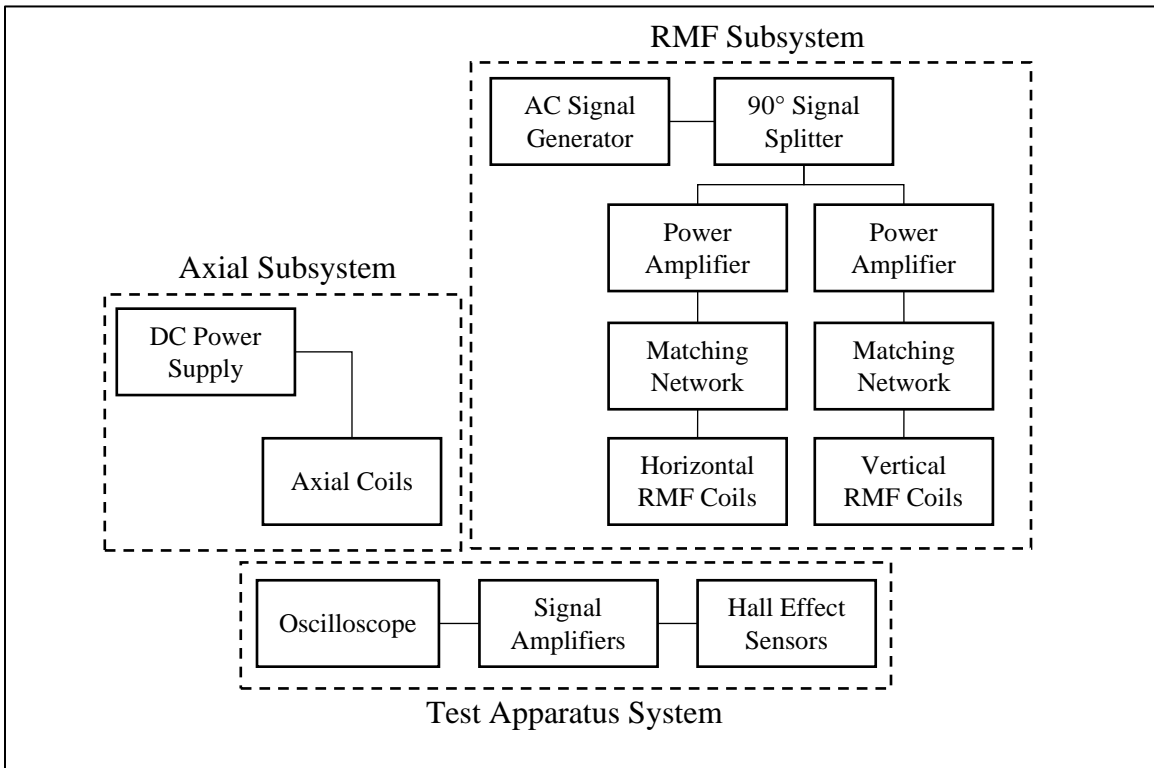


Figure 1.3 – Prototype system block diagram.

2 Simulation Environment

2.1 Introduction

Plasma physics often includes the effects of physical phenomena that are neglected in other disciplines. Because of this, it was necessary to verify that the simulation environment used in this project was capable of modeling these effects. The phenomena involved in FRC formation were particularly important to capture, because these effects are heavily involved in thrust production.

2.2 Software Selection

The simulation software chosen as a candidate for this project was the CFD software STAR-CCM+. This software was primarily considered for two reasons. The first reason was that STAR-CCM+ has multiphysics models for electromagnetism and MHD, and it has documentation for simulating plasma. The second reason was that the license for this software was accessible through SJSU.

2.3 Software Validation

2.3.1 Goals

The validation objective for the selected simulation software was to demonstrate that it could effectively capture plasma behavior associated with FRC formation. The main behavior that was looked for was a rotational current density in the plane of the rotating magnetic field. The interaction of this azimuthal current density with a diverging axial magnetic field is the main method of thrust production in the RMF thruster scheme. This is why this rotational current density was the main behavior of interest.

2.3.2 Geometry

The geometry used for the validation study was based on the Rotamak configuration used in the NTU plasma generation experiment. As noted in Chapter 1, this configuration is not capable of producing thrust. Thrust production was not necessary for the validation simulations because they were focused only on capturing plasma behavior in a rotating magnetic field.

An image of the final geometry used in the validation simulations is shown in Figure 2.1. The plasma containment region was a sphere with a diameter of 28 cm. The coordinate system was Cartesian, with the origin at the center of the sphere. The electromagnetic coils were configured such that the steady axial magnetic field was in the direction of the x-axis, and the rotating magnetic field was in the y-z plane.

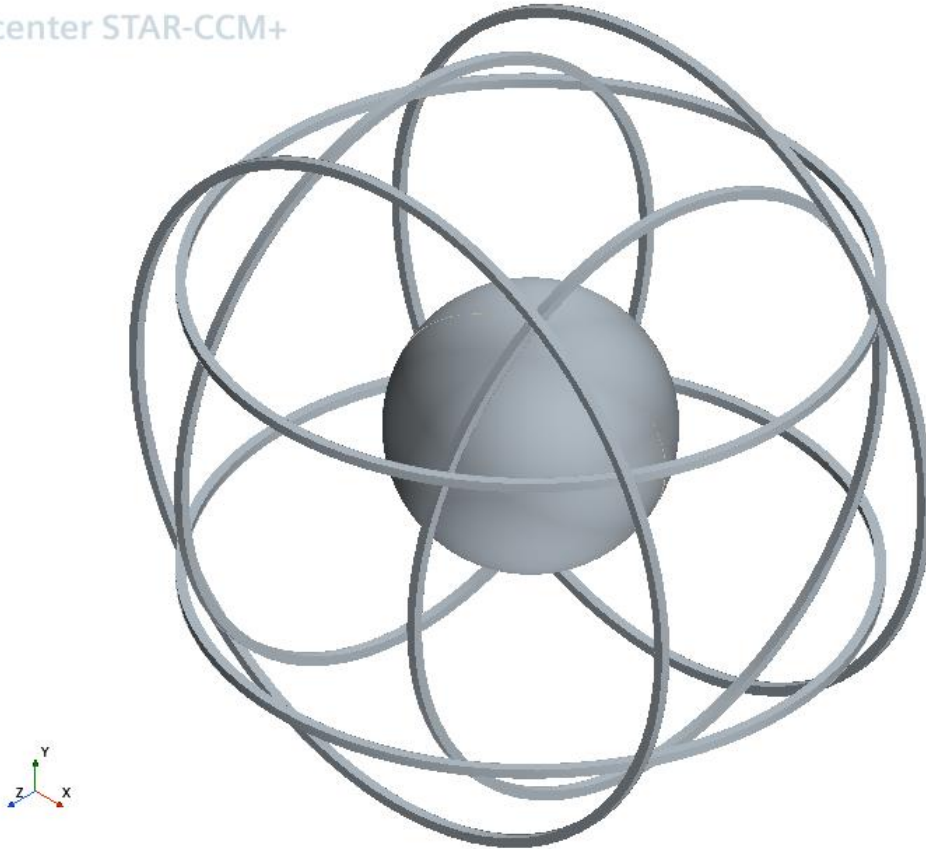


Figure 2.1 – Geometry used in the validation study simulations.

The coils used in this geometry were much larger than the plasma containment vessel. Initial versions of the simulation geometry used smaller coils that were closer in diameter to the sphere. However, this caused the magnetic field strength to vary significantly throughout the plasma vessel. This resulted in small regions of high magnetic field strength, and these hot spots caused instability in the simulation. Because of this, the coils were resized into larger Helmholtz coils to reduce magnetic field strength variance in the plasma vessel.

2.3.3 Mesh

In the validation simulations, the plasma vessel was discretized using a 3D polyhedral mesh with a cell count of approximately 1.3 million. A cross section of the plasma vessel mesh is shown in Figure 2.2. It is likely that this mesh was not large enough for numerical simulation results to be independent of the mesh size. However, this validation study focused on demonstrating the presence of bulk physics phenomena at length scales similar to the simulation domain. Additionally, the validation study involved many values of many variables, which resulted in a large number of simulation configurations that needed to be run. Because of these factors, computation time was prioritized over numerical precision when generating the mesh.

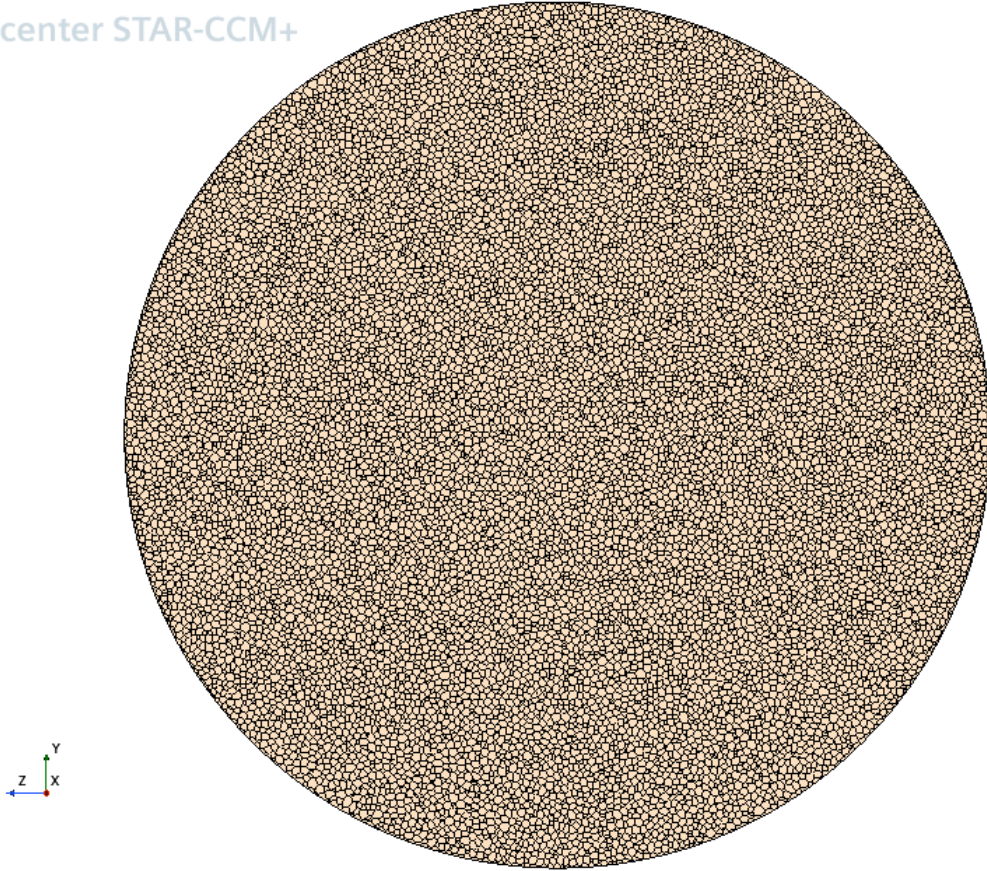


Figure 2.2 – Cross-section of the plasma vessel mesh.

2.3.4 Physics Modeling

In the simulation software, electromagnetic, viscous fluid flow, and magnetohydrodynamic models were used to provide governing equations for the plasma flow. The ideal gas law was used as the equation of state. The simulations were run using a time-dependent solver. The time step was set to one eighth of the period of the rotating magnetic field.

After several simulation runs did not provide desired results, it was determined that STAR-CCM+ uses a form of Ohm's law given by Eq. (2.1).

$$\mathbf{E} = \eta \mathbf{J} \quad (2.1)$$

This is the standard form of Ohm's law that is typically used in electromagnetic applications. However, the plasma physics under consideration in this project require an extended form of Ohm's law given by Eq. (2.2).

$$\mathbf{E} = \eta \mathbf{J} + \frac{1}{n_e q_e} \mathbf{J} \times \mathbf{B} \quad (2.2)$$

The cross product on the right-hand side, called the Hall term, is necessary to model the physics involved in FRC formation. (Notably, Eq. (1.1) is a modified version of this extended Ohm's

law.) To correct the issue, a user defined function for the Hall term was added to the STAR-CCM+ electromagnetics model.

The working fluid for the validation study was Argon. Argon was chosen for this study because it was used as the plasma medium in the NTU proof of concept experiment. The initial conditions for the fluid in the final simulation case were a temperature of 300 K, a pressure of 0.5 Pa, and a velocity of 0 m/s.

The magnetic fields were generated using excitation coil models. The axial coils were assigned a constant DC current. The RMF coils were assigned time-varying sinusoidal currents phase shifted by 90 degrees between each pair. The current magnitude and number of turns in all three coil pairs were varied over the course of the validation study to vary the magnetic field strength in the plasma vessel. The frequency and rotation direction of the rotating magnetic field were also varied.**Error! Reference source not found.**

2.3.5 Results

In the final simulation case, the current density vector field displayed a rotational component in the y-z plane. A vector field plot of this rotational component is shown in Figure 2.3. This simulation case was run for 27 time steps, corresponding to 3.375 RMF periods. The rotational current density component remained present throughout the entire simulation time. As discussed in Section 2.3.3, the numerical values of this current density field component may not be entirely physically accurate. However, these values are on a similar order of magnitude to values found in literature concerning FRC formation.

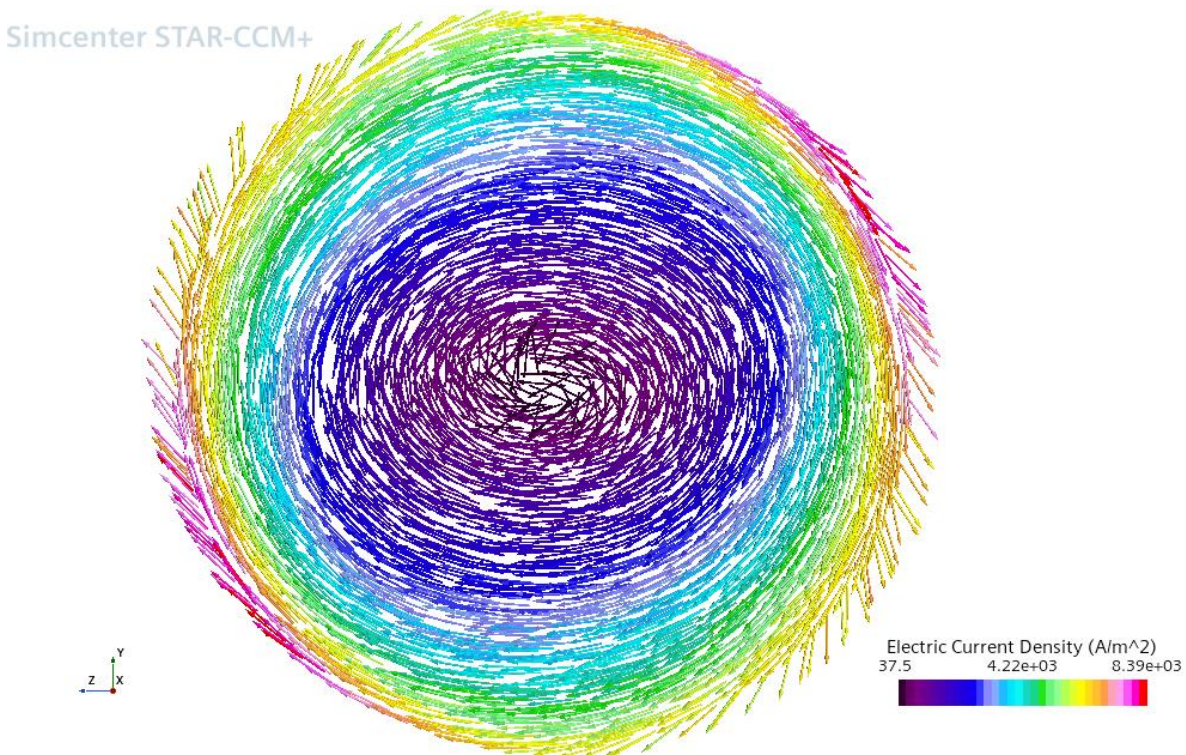


Figure 2.3 – Component of current density tangent to the y-z plane.

In Figure 2.3, the positive x-axis points out of the page. From this perspective, the RMF rotates in the counterclockwise direction. The rotational current density component is in the opposite direction, which is the expected behavior. As discussed in Section 1.2, the RMF causes electrons to revolve in the direction of the RMF, and the current density is in the opposite direction of electron motion. Additionally, this clockwise current density component would produce a magnetic field in the negative x-direction, which is the opposite direction of the applied axial magnetic field. This is another expected behavior associated with FRC formation.

When the RMF was set to rotate counterclockwise, a rotational current density was produced in a direction that countered the applied axial magnetic field. However, in simulation cases where the RMF was set to rotate clockwise, no rotational current density was produced at all. This suggests two things. One is that the RMF is responsible for the production of the rotational current density in the simulation. The other is that the rotational current density must oppose the applied axial magnetic field in order to be produced. These simulation behaviors both correspond to physical mechanisms associated with FRC formation. In general, the results of the validation study signify that this simulation environment is suitable for modeling the desired plasma behavior.

An additional result of the validation study was an observed temperature increase in the plasma vessel. As stated in Section 2.3.4, the initial temperature in the plasma vessel was 300 K. By the final time step, the temperature had risen to values in the thousands of kelvins throughout the vessel. A scalar field plot of the temperature profile at the final time step is shown in Figure 2.4. It should be noted that plasma temperature is typically a more complex parameter than bulk fluid temperature. However, this temperature increase still suggests that the simulation environment can effectively simulate the ionization of the plasma by the RMF.

Simcenter STAR-CCM+

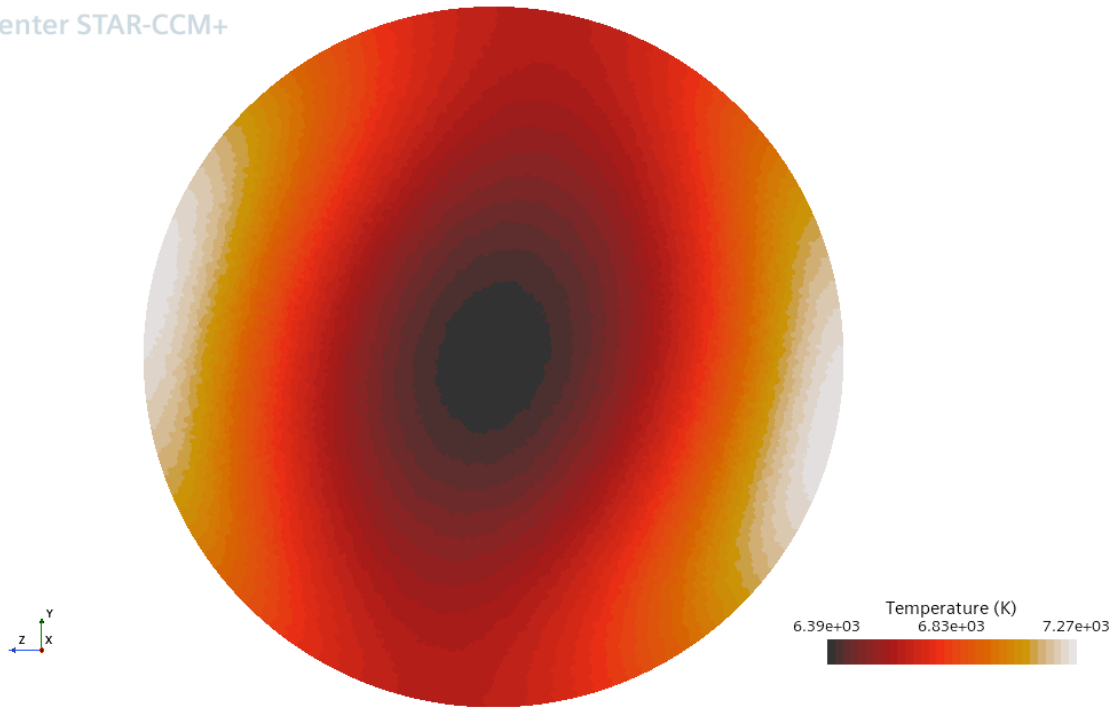


Figure 2.4 – Cross-section of the temperature profile in the plasma vessel.

3 Thruster Simulations

3.1 Geometry

3.1.1 Thruster Body

The first step in performing the thruster simulations was designing the thruster body itself. A constant-diameter cylindrical tube was chosen for the shape of the thruster. It is possible that incorporating a nozzle into the thruster body would improve the performance of the thruster. However, this study is primarily concerned with the thrust produced from the electromagnetic coil array. Incorporating thrust produced by a nozzle would complicate the process of evaluating the performance of the electromagnetic configurations on their own. Investigating the relationship between electromagnetic thrust performance and conventional rocket nozzle design is suggested as a topic for future work.

Many scales were considered for the thruster body, but the scale chosen for study was a diameter of 10 cm. This scale was chosen for two reasons. The first reason was to investigate plasma characteristics at a scale smaller than the one used in the NTU experiment. The second reason was to allow the electromagnetic coils to be relatively larger than the thruster body without making the entire thruster array prohibitively large for a small spacecraft. Making the electromagnetic coils larger than the thruster body is desirable because it increases the uniformity of the magnetic field within the thruster.

The thruster body design used in the simulations is shown in Figure 3.1. The thruster body has a diameter of 10 cm, and a length of 30 cm. The axis of the cylinder is aligned with the x-axis of the simulation coordinate system, with the direction of flow in the positive x-direction. The radial-tangential plane of the cylinder is aligned with the y-z plane of the simulation coordinate system.

Simcenter STAR-CCM+

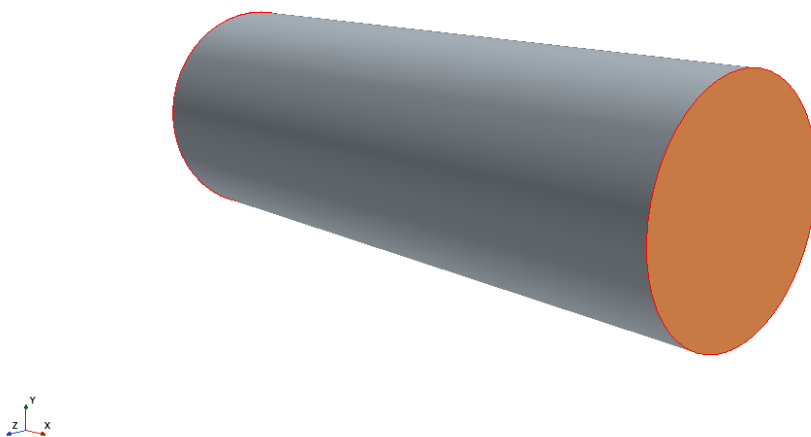


Figure 3.1 – Thruster body geometry.

3.1.2 RMF Coils

The RMF coil design used in the thruster simulations is shown in Figure 3.2. The curved profile was chosen to reduce the size of the effective envelope of the RMF coil array. Because of this, the RMF coil array was able to fit inside the inner diameter of the axial coils without making the axial coils prohibitively large.

Simcenter STAR-CCM+

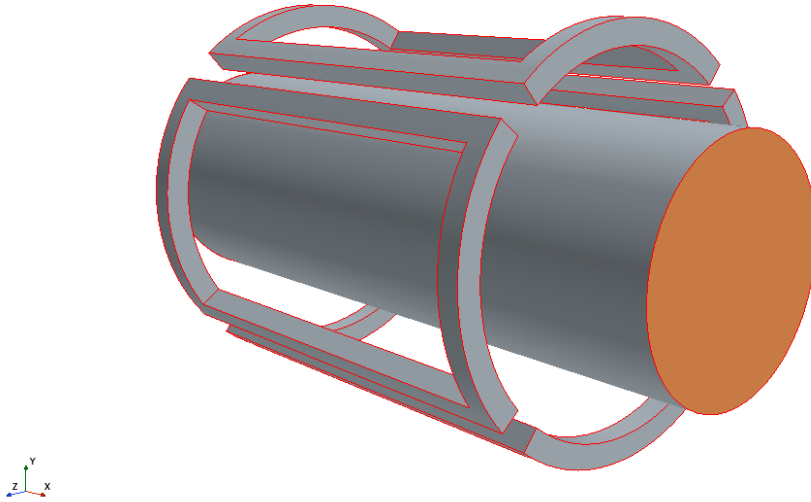


Figure 3.2 – RMF coil array geometry.

3.1.3 Axial Coil Configurations

Comparing the performance of different axial coil configurations is the primary objective of the thruster simulations. For an axial coil configuration to be useful for thrust production, it must produce an axial magnetic field with a component in the outward radial direction, as discussed in Chapter 1. This is typically done with an asymmetric axial coil array.

The first configuration chosen for the simulations is a configuration with no axial coils. This configuration was named the RMF Only configuration. The RMF Only configuration was chosen to study the performance of the thruster in the purely electrothermal mode, without significant Lorentz force in the flow direction. The RMF Only configuration is shown in Figure 3.3.

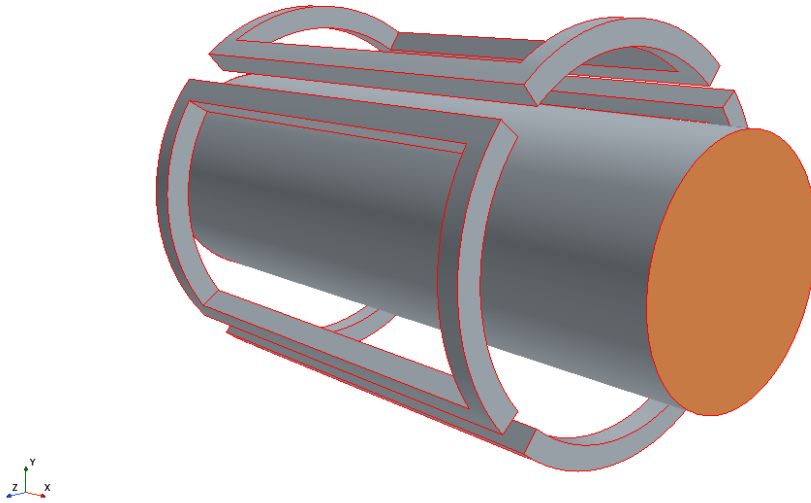


Figure 3.3 – RMF Only thruster configuration.

The second configuration uses a single axial coil near the inlet side of the RMF coils. This configuration was named the Single Coil configuration. The magnetic field lines of a single coil diverge outward as the distance from the coil increases. This produces the necessary radial component of the axial magnetic field. The Single Coil configuration is shown in Figure 3.4.

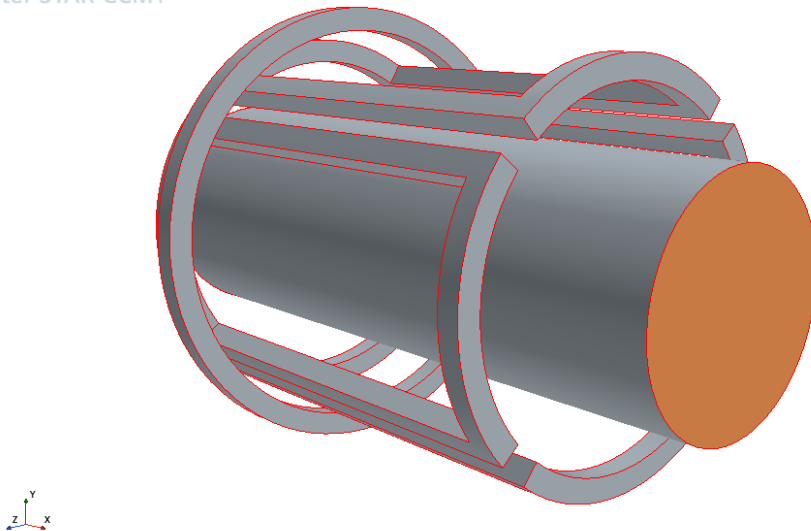


Figure 3.4 – Single Coil thruster configuration.

The third and fourth configurations both use two axial coils. The third configuration uses two coils of different sizes, but with the same electric current. This configuration was named the Varying Size configuration. The fourth configuration uses two axial coils of the same size but

with different electric currents. This configuration was named the Varying Current configuration. Both of these configurations essentially augment the magnetic field of the Single Coil configuration with a second coil. This second coil increases the magnetic field strength at locations far from the first coil. However, the second coil generates a weaker magnetic field than the first coil so that the net radial component of the magnetic field is still outward. The Varying Size configuration is shown in Figure 3.5. The Varying Current configuration is shown in Figure 3.6.

Simcenter STAR-CCM+

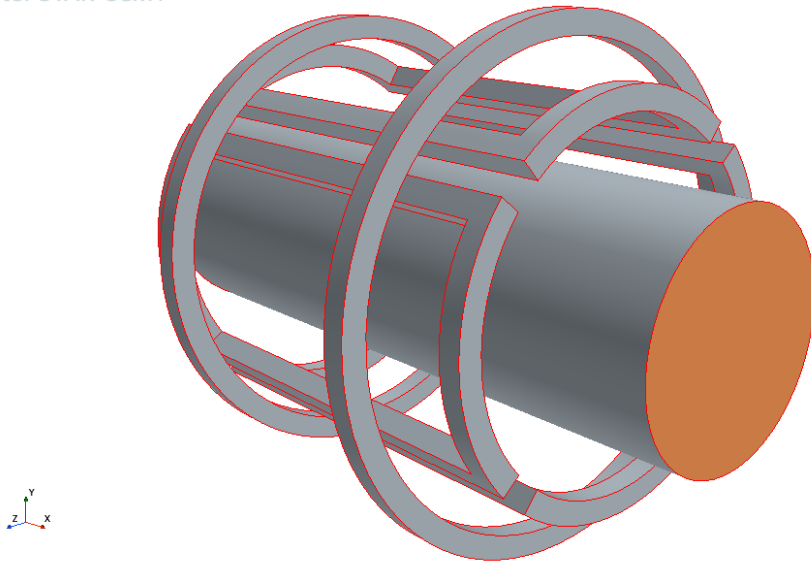


Figure 3.5 – Varying Size thruster configuration.

Simcenter STAR-CCM+

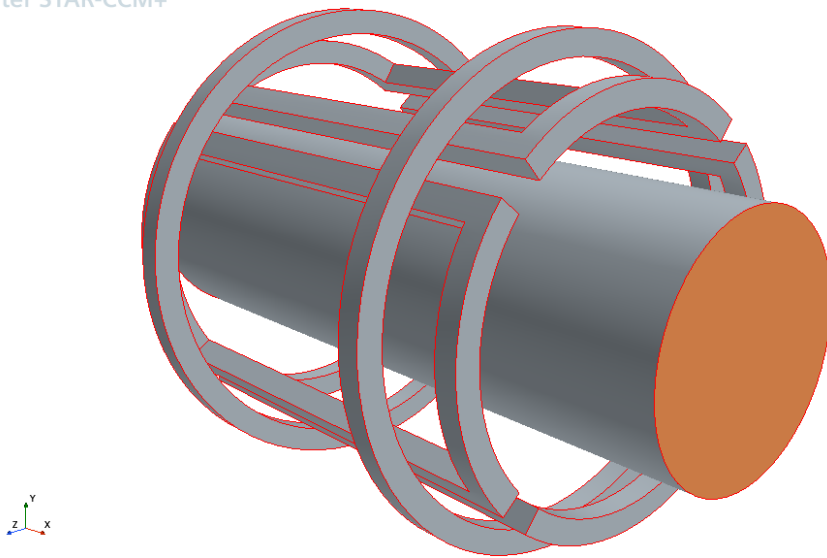


Figure 3.6 – Varying Current thruster configuration.

The fifth configuration uses a single coil that expands along the length of the thruster. This configuration was named the Mini-ELF configuration. A similar axial coil configuration was used in the ELF thruster concept described in Section 1.2. However, the configuration used in this project is on a smaller scale than the ELF thruster. The Mini-ELF configuration is shown in Figure 3.7.

Simcenter STAR-CCM+

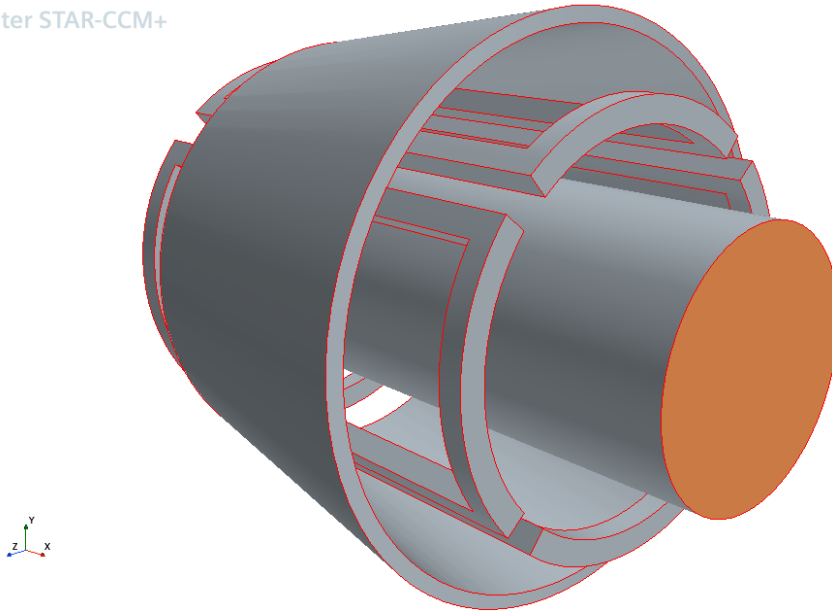


Figure 3.7 – Mini-ELF thruster configuration.

3.2 Mesh

In the thruster simulations, the thruster body was discretized with a polyhedral mesh with a cell count of approximately 2.8 million. Cross sections of the thruster body mesh in the x-y and y-z planes are shown in Figure 3.8 and Figure 3.9, respectively.



Figure 3.8 – Cross section of the thruster mesh in the x-y plane.



Figure 3.9 – Cross section of the thruster mesh in the y-z plane.

3.3 Physics Modeling

The models used for the thruster simulations were similar to the ones used in the simulation environment described in Chapter 2. However, an inviscid fluid flow model was used, rather than a viscous model. This is because viscous effects were not considered to be a significant factor in studying the thruster performance of the electromagnetic coil arrays. Electromagnetic and magnetohydrodynamic models were also used, and the user defined Hall term discussed in Section 2.3.4 was implemented as well. The ideal gas law was used as the equation of state. A time dependent solver was used, with the time step set to one eighth of the period of the rotating magnetic field.

Argon was used as the working fluid for the thruster simulations. Argon was chosen because its plasma behavior was able to be sufficiently modeled in the validation study. The initial conditions of the fluid were a pressure of 0.5 Pa, a temperature of 300 K, and a velocity of 0.1 m/s in the positive x-direction.

The electromagnetic coil configurations were simulated with excitation coil models. The axial coils used a steady DC current. The RMF coils used time-varying sinusoidal currents that were phase shifted 90 degrees between each pair. All of the axial coil configurations had a total of 20 turns. Every axial coil configuration used a current magnitude of 6 A, with the exception of the secondary coil of the Varying Current configuration, which used a current magnitude of 4 A. The RMF coils had 25 turns per coil, equating to 50 turns per coil pair. The RMF coils used a current amplitude of 6 A. The frequency used for the RMF coils was 350.1 kHz, which corresponds to an angular frequency of $2.2 \cdot 10^6$ rad/s. This frequency was the frequency used in the final simulation case of the validation study.

3.4 Results and Discussion

3.4.1 Electromagnetic Characteristics

All of the thruster configurations developed components of current density in the y-z plane that were oriented in the clockwise direction. However, these current density components were not fully rotational, which suggests that none of the configurations were fully operating in the FRC regime. An example of the component of the current density field tangent to the y-z plane is shown in Figure 3.10. The shape of the field shown in Figure 3.10 is typical of all the thruster configurations.

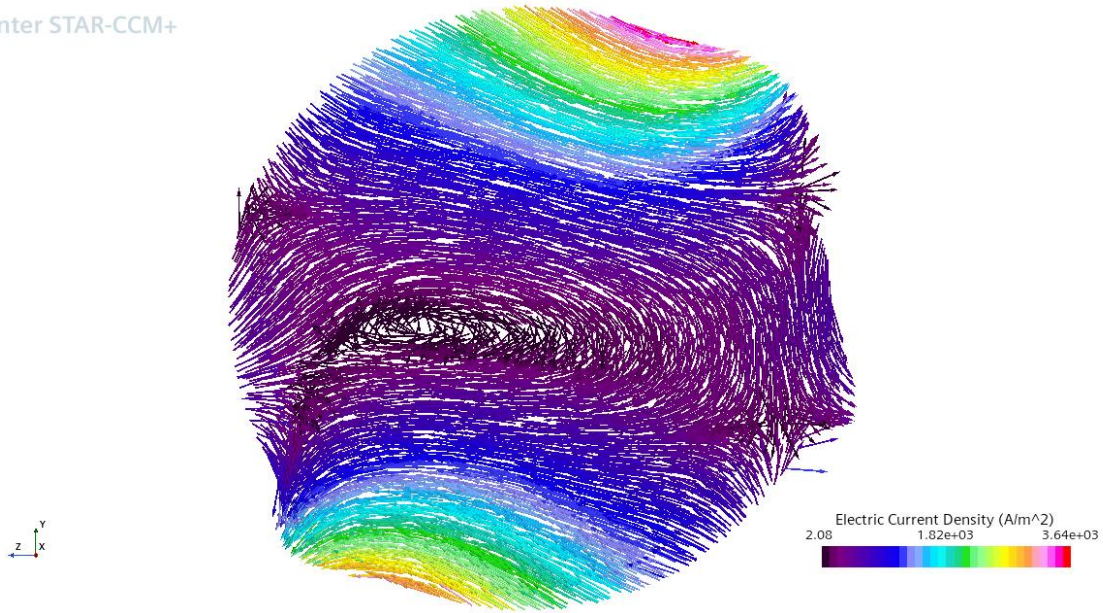


Figure 3.10 – Component of current density tangent to the y-z plane.

The x-component of the net Lorentz force was measured from the simulations as a numerical measure of the electromagnetic performance of the thruster. While the thruster configurations were not operating in the FRC regime in these simulations, there was still a component of Lorentz force in the positive x-direction for all the thruster configurations. The differences in these values between configurations could be considered an estimate of how these configurations might perform relative to each other when operating in the FRC regime. The measured net Lorentz force values in the flow direction for each thruster configuration are shown in Table 3.1.

Table 3.1 – Net Lorentz force in the x-direction.

Configuration	Net Lorentz Force
RMF Only	0.108 mN
Single Coil	0.0936 mN
Varying Size	0.122 mN
Varying Current	0.119 mN
Mini-ELF	0.126 mN

3.4.2 Thruster Performance

Thrust and mass flow rate values for the thruster were measured from the simulations. These measured parameters were used to calculate the specific impulse of each thruster configuration. Since the results of these simulations have not been validated with physical testing, it is not considered meaningful to compare these performance parameters to physically validated performance parameters of existing EPT systems. However, it is considered meaningful to use them as relative comparison metrics for the different coil configurations, and comparing the configurations is the main objective of the simulation phase of the project. To reflect that these performance parameters are only meaningful relative to each other, they have been presented in

nondimensional form. The nondimensionalization was performed by dividing the dimensional values by the values of a base case. The RMF only values were chosen as the base case.

The nondimensionalized thrust and specific impulse of each thruster configuration are shown in Table 3.2. For documentation purposes, the dimensional values for the RMF Only configuration were a thrust of 4.484 mN and a specific impulse of 1245 s. The dimensional values for any other configuration can be obtained by multiplying the nondimensional values by the values for the RMF Only configuration.

Table 3.2 – Nondimensional thruster performance parameters.

Configuration	Nondimensional Thrust	Nondimensional Specific Impulse
RMF Only	1.0000	1.0000
Single Coil	1.0004	0.9855
Varying Size	1.0035	0.9470
Varying Current	1.0012	0.9798
Mini-ELF	1.0007	0.9826

The thrust and specific impulse values are similar across all configurations, including the configuration without axial coils. This agrees with the hypothesis presented in Section 3.4.1 that the thruster was not operating in the FRC regime in these simulations. Instead, it was likely operating in the electrothermal regime, where thrust is primarily produced from the heating of the plasma. Because all the configurations use the same RMF coil array to ionize the plasma, it makes sense that all of them would have similar performance when operating in the electrothermal regime.

3.4.3 Electrical Power Requirements

In the STAR-CCM+ simulations of the thruster, the only required electrical parameter for the electromagnetic coils is the current. Current alone is not enough to estimate electric power requirements for the RMF coils. This is because the RMF coils use alternating current, and so the reactance of the coils must be accounted for. The circuit analysis software LTspice was used to model the equivalent circuit of the RMF coils. Lumped parameters of the equivalent circuit elements, specifically inductance and resistance, were calculated from measurements of coil magnetic flux linkage and conductor resistance from the STAR-CCM+ simulations.

Since the coils are modeled as inductors in the equivalent circuit, their impedance is almost entirely reactive. Because of this, most of the power in the circuit is reactive power. The total apparent power input for the coils significantly exceeded the power input requirement threshold of 1 kW. To resolve this issue, a capacitor sized to match the reactance of the coils was added in series with the coil circuit. This reduces the reactive power seen by the source, which reduces the required input power for the coil circuit. Additionally, the power dissipated into the plasma is modeled as a resistance in the circuit. The value of this resistance was estimated from literature [23]. A diagram of the RMF coil circuit with the series capacitor and the equivalent plasma resistance is shown in Figure 3.11.

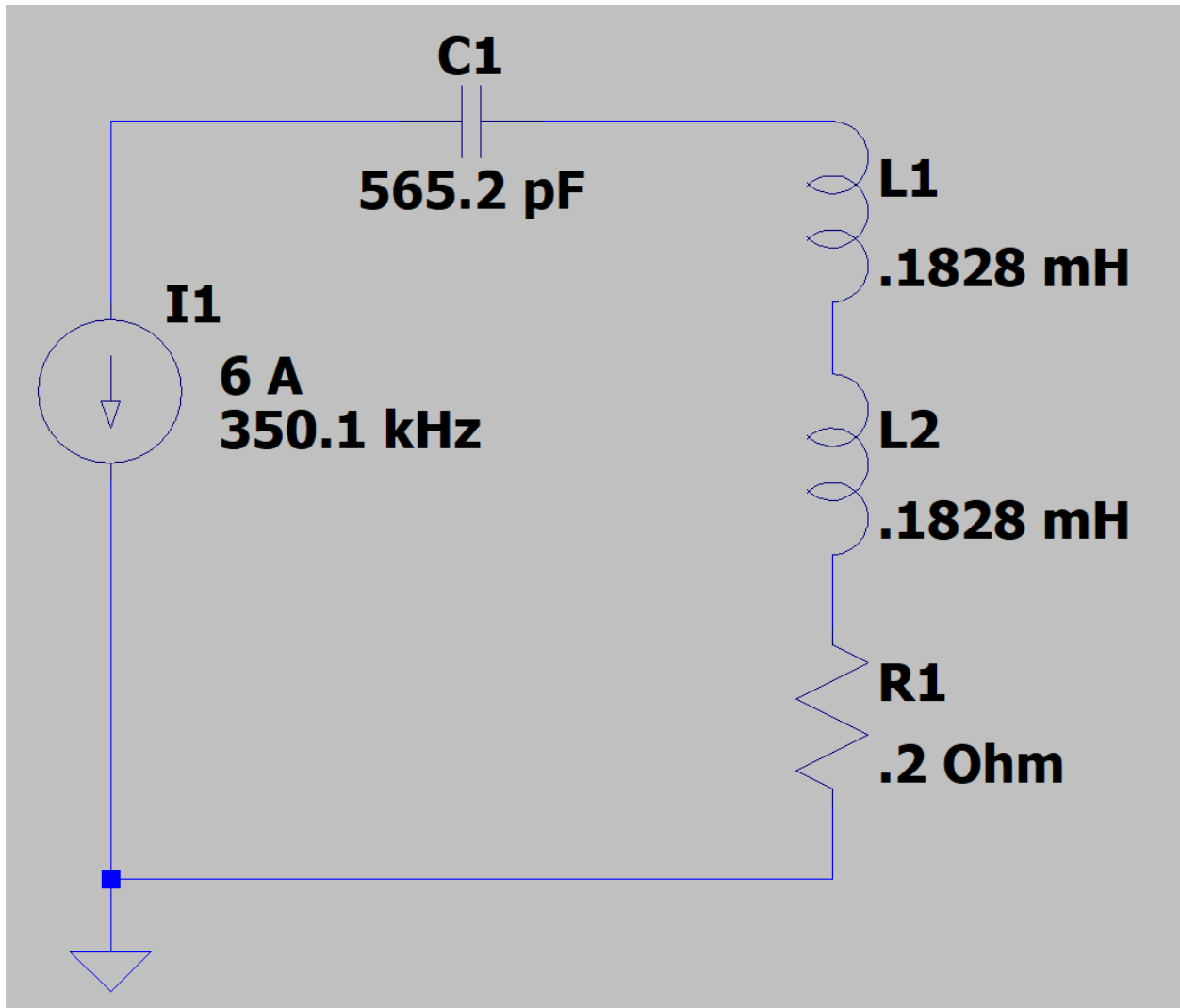


Figure 3.11 – RMF coil equivalent circuit diagram.

The required input power for the RMF coils was determined from the steady state apparent power seen by the source in the LTspice circuit simulations. Since the axial coils use direct current, the required input power for them was able to be calculated analytically from the current and the resistance of the coils. Total input power requirements and the thrust to power ratio for each configuration are shown in Table 3.3.

Table 3.3 – Thruster electrical performance parameters.

Configuration	Input Power	Thrust to Power Ratio
RMF Only	480.0 W	9.34 mN/kW
Single Coil	482.4 W	9.30 mN/kW
Varying Size	482.5 W	9.33 mN/kW
Varying Current	481.7 W	9.32 mN/kW
Mini-ELF	482.5 W	9.30 mN/kW

The largest component of the required input power values is contributed by the RMF coils. The power required for the RMF coils is 480 W, while the power required for the axial coils in any configuration is in the range of 2 W. This large difference in required power is because, despite the power factor correction capacitor, the voltage and current seen by the source were not completely in phase in the LTspice circuit simulations. Physical testing of the RMF coil circuit impedance will need to be performed to determine if the presence of this much reactive power is physically accurate.

For the purposes of thruster configuration comparison, it can be assumed that the power required for the RMF coils is the same between all configurations. This is because all of the thruster configurations use the same RMF coil array. The only differences in power requirements between configurations would then come from the power requirements for the axial coils. The axial coil power requirements for each thruster configuration are shown in Table 3.4.

Table 3.4 – Input power required for the axial coils.

Configuration	Axial Coil Input Power
RMF Only	0 W
Single Coil	2.37 W
Varying Size	2.50 W
Varying Current	1.71 W
Mini-ELF	2.50 W

3.4.4 Configuration Selection

Since the measured thruster performance parameters are so similar between configurations, it is not feasible to choose an optimal configuration based on these parameters. Because of this, other factors need to be considered. As discussed in Section 3.4.1, the net Lorentz force in the flow direction was measured for each thruster configuration. While this force is not a significant contribution to the thrust in the conditions simulated, the relative differences between these Lorentz force values can be used to compare how the different configurations might perform in the FRC regime.

The Lorentz force contributed by the axial coils is the main quantity of interest for the purpose of configuration selection. This parameter can be calculated by subtracting the Lorentz force contributed by the RMF coils from the total Lorentz force value. The Lorentz force value measured from the RMF only configuration can be considered to be the Lorentz force contributed by the RMF coils for this purpose.

The power input required for the axial coils is another parameter of use for configuration selection. The input power required for each axial coil configuration was discussed in Section 3.4.3 and shown in Table 3.4. Using the parameters discussed, an optimal coil configuration would generate the most Lorentz force using the least input power. Based on this, the ratio of Lorentz force to input power is another performance parameter to be considered for configuration selection.

The net x-direction Lorentz force, input power, and ratio of Lorentz force to input power for each axial coil configuration is shown in Table 3.5. The Single Coil configuration had a smaller total axial Lorentz force than the RMF Only configuration, which suggests that the net Lorentz force produced by the axial coil opposes the flow. Of the configurations tested, the Mini-ELF configuration provides the best ratio of Lorentz force to input power. Because of this, the Mini-ELF configuration has been selected for the prototype phase.

Table 3.5 – Axial coil x-direction Lorentz force and input power.

Configuration	Axial Coil Lorentz Force	Axial Coil Input Power	Axial Coil Lorentz Force to Input Power Ratio
RMF Only	0 mN	0 W	N/A
Single Coil	-0.0148 mN	2.37 W	N/A
Varying Size	0.0131 mN	2.50 W	5.26 mN/kW
Varying Current	0.0105 mN	1.71 W	6.11 mN/kW
Mini-ELF	0.0180 mN	2.50 W	7.21 mN/kW

4 Prototype Design – RMF Generation

4.1 Introduction

With a coil configuration selected from the simulations, the next phase of the project was to begin constructing a physical prototype of that coil configuration. The first part of the prototype that was constructed was the RMF generation system. The method of RMF generation selected for the prototype was the same type of orthogonal coil configuration used in the simulations of Chapter 2 and Chapter 3. As discussed in Chapter 1, this method of RMF generation is what is typically used in rotating magnetic field thrusters.

There are two components that are necessary for this RMF generation method. The first component is two identical sets of magnetic coils that are positioned orthogonally from each other. The second component is a method of generating two identical, sinusoidal AC signals that are phase shifted from each other by 90 degrees.

4.2 Signal Generation

The target frequency selected for the rotating magnetic field was 350 kHz. This is the same frequency that was used in the simulations of Chapter 2 and Chapter 3. The signal generation method selected for this project was a circuit based on an XR2206 function generator integrated circuit. This method was selected because the XR2206 IC provided suitable frequency range and signal accuracy at a much lower cost than a benchtop function generator unit. The basis of the signal generator circuit used in this project was obtained from the datasheet of the XR2206 [24]. This circuit is shown in Figure 4.1.

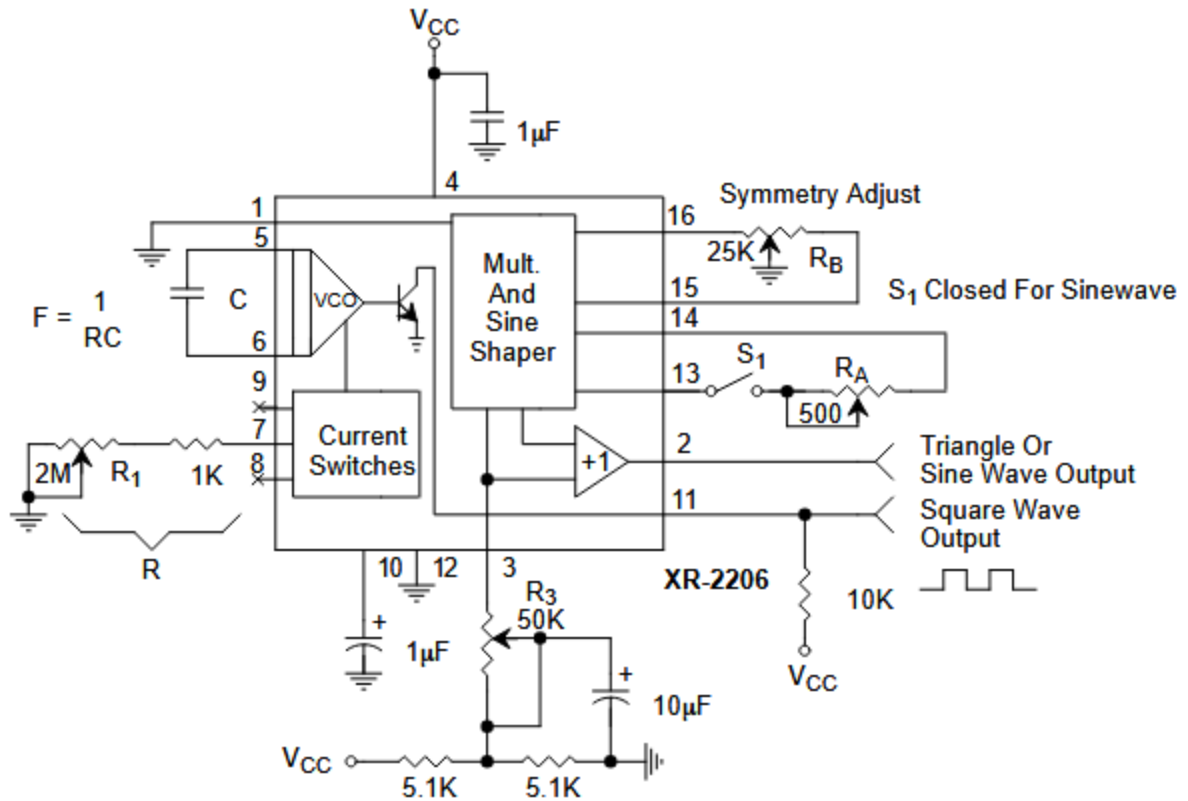


Figure 4.1 – Signal generator circuit from the XR2206 datasheet [24].

As shown in Figure 4.1, the frequency of the output signal is given by Eq. (4.1).

$$f = \frac{1}{RC} \quad (4.1)$$

In Eq. (4.1), C is the capacitance of the capacitor connected to pins 5 and 6, and R is the total resistance of the resistors connected to pin 7. For this project, a value of 1000 pF was chosen for C , since this was the minimum capacitance value recommended by the datasheet [24]. To achieve a frequency of 350 kHz with this capacitance value, a resistance of approximately 2857 Ω was needed. To accomplish this, the 2 M Ω potentiometer shown in Figure 4.1 was replaced with a 25 k Ω potentiometer. This modification was made because the 2 M Ω potentiometer was not able to be set precisely to such a relatively small resistance value.

Additional circuitry was added to the sine wave output pin. The first addition was an RC high pass filter. This circuit was added because it was found that the output of the signal generator circuit had a DC bias. The capacitor of the filter acts as a coupling capacitor to remove the DC bias. The time constant of the filter was set so that the cutoff frequency was approximately 80 kHz. This cutoff frequency was chosen to be sufficiently lower than the frequency of the output signal.

The second addition to the output pin was an RC-CR network. This network splits an input sinusoidal signal into two output signals that are phase shifted from each other by 90 degrees [25]. The time constant of this network was chosen so that the pole frequency would be nearly equal to the signal frequency of 350 kHz. When the pole frequency equals the signal frequency, both outputs have equal amplitude [25]. This network was added to provide the 90° phase shifted output signals necessary for RMF generation.

A circuit diagram of the RC high pass filter and RC-CR network is shown in Figure 4.2. The high pass filter is on the left side of the diagram. It consists of a series capacitor and a shunt resistor. The RC-CR network is on the right side of the diagram. The top branch consists of a series resistor with a shunt capacitor, and the bottom branch consists of a series capacitor with a shunt resistor. Both branches have the same resistance and capacitance values. The output of the bottom branch is phase shifted by +90° from the output of the top branch. This means that the top branch can be considered a sine output, and the bottom branch can be considered a cosine output.

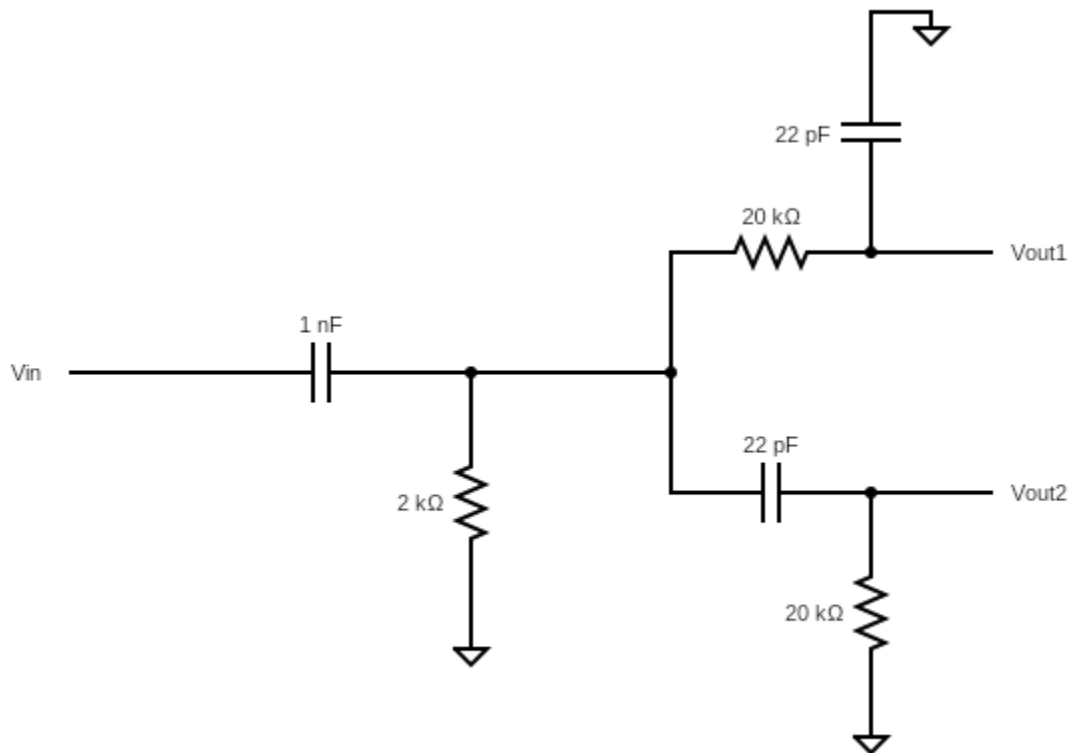


Figure 4.2 – High pass filter and phase splitter circuit diagram.

The circuit was initially assembled on a solderless breadboard for ease of modification while testing. An image of the assembled circuit, including the signal generator, filter, and phase shift splitter network, is shown in Figure 4.3. The output of this circuit was tested with an oscilloscope, and the results of this testing are discussed in Section 4.4.1.

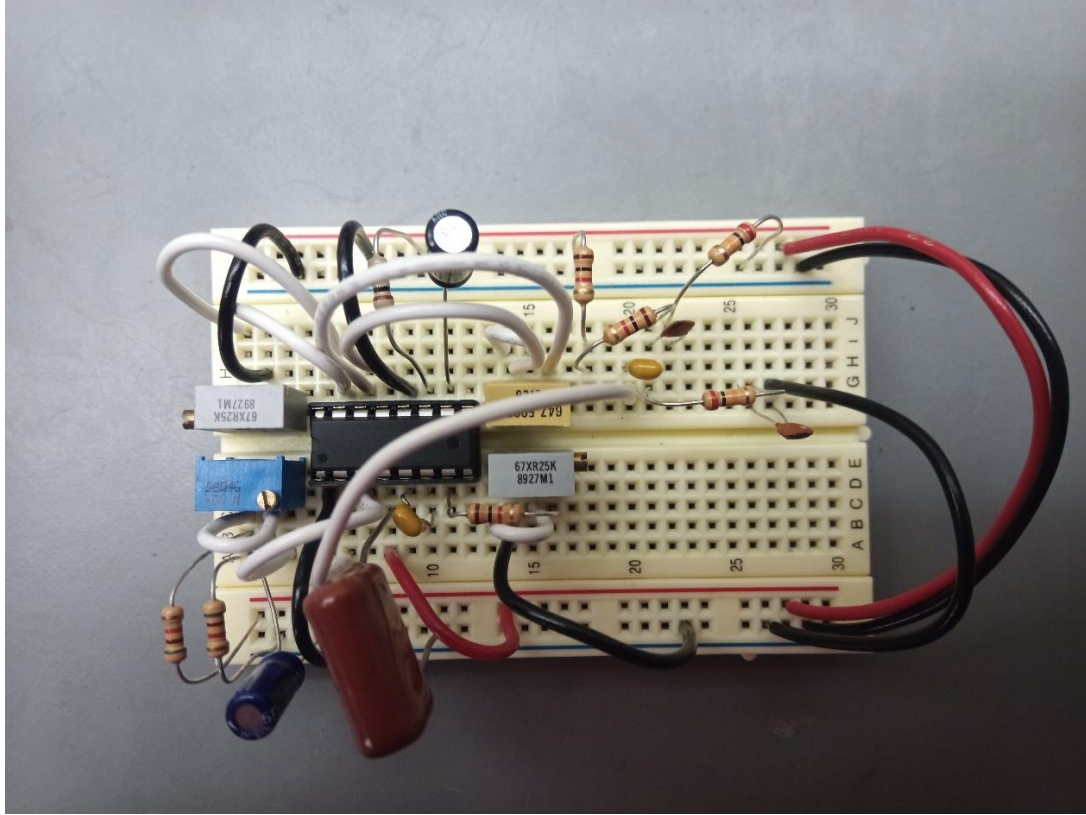


Figure 4.3 – The assembled signal generator circuit.

4.3 RMF Coil Design

In the thruster simulations of Chapter 3, the RMF coils were designed with a rectangular shape that was curved to follow the surface of the cylindrical thruster body. This shape was chosen to reduce the effective envelope of the RMF coil array, which would allow the axial coils to more easily fit around the RMF coils. To maintain this benefit, the same type of curved rectangular design was chosen for the RMF coils of the prototype.

To achieve this shape, the RMF coils were wound around pegs mounted into the surface of a cylindrical tube. It should be noted that this tube was not intended to act as a thrust chamber. This prototype was only intended for vacuum magnetic field testing of the coils in the absence of plasma. Because of this, there were no requirements made for the structural elements to withstand and contain plasma. Considering that, the only major requirements for the structural elements were as follows:

- The structure must be capable of maintaining the shape and position of the coils.
- The structure must be non-conductive and non-magnetic to prevent interference with the electrical and magnetic characteristics of the coils.

The scaffold structure was constructed from a tube made of ABS plastic. The tube section used for this scaffold had a length of 12 cm and an outer diameter of 6 cm. The tube had a thickness of approximately 0.4 cm. Wooden pegs were mounted to the tube to act as posts for coil windings. These pegs had a diameter of approximately 0.48 cm and a length of

approximately 1.4 cm. These pegs were fastened into holes in the tube body with epoxy resin. The mounting posts were located so that each coil would sweep out an angle of 62° along the circumference of the cylinder and have a length of 7 cm along the length of the cylinder. A mounting post was inserted at each corner of this desired coil shape, with an inward offset made for the radius of the posts. This arrangement of four posts was repeated at 90° intervals along the circumference of the cylinder to create two orthogonal coil pairs.

Two additional holes were added to the bottom surface of the cylinder. These holes had a diameter of approximately 0.95 cm, and their centers were located 1 cm from the edges of the cylinder. These holes were added to act as mounting points to attach the RMF coil array to a base. A schematic drawing of the scaffold tube showing the winding post and mounting point hole locations is shown in Figure 4.4.

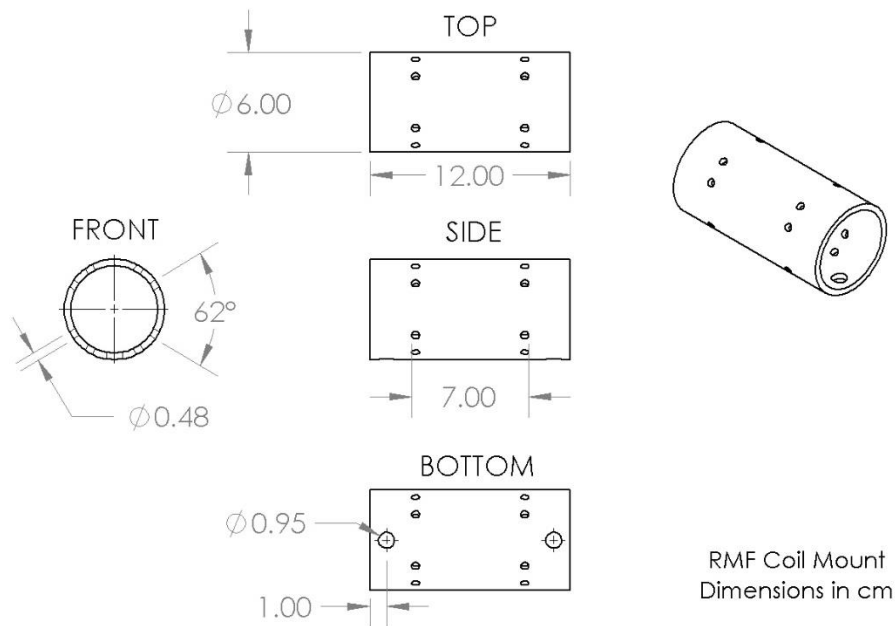


Figure 4.4 – Schematic diagram of the RMF coil array scaffold tube.

For the design of the coil windings, resistive heating was a potential concern. To generate a significant magnetic field, high current is typically needed, and this could cause significant power dissipation if the coils had relatively high resistance. To reduce resistance of the coils, they were wound using a small turn count and wire with a relatively high thickness. Each coil was wound from five turns of 16 AWG enameled copper magnet wire, which resulted in 10 turns per connected coil pair.

Several images of the wound coils are shown in Figure 4.5 through Figure 4.7. As required for RMF generation, the coil pairs were arranged perpendicular to each other. Each individual coil was connected in series to the paired coil on the opposite side of the array. This was done due to it being the simplest method of ensuring that each coil in a pair had the same current through it.



Figure 4.5 – Top view of the RMF coil array.



Figure 4.6 – Side view of the RMF coil array.



Figure 4.7 – Perspective view of the RMF coil array.

Because the RMF coils use AC input, they functionally act like inductors. Since inductors are reactive components, the RMF coils would introduce significant amounts of reactive power into the circuit. While reactive power does not do physical work, an equivalent amount of apparent power must still be supplied to the circuit to account for it. Because of this, for a circuit with a fixed target current, the addition of a reactive component requires the source to provide more power to achieve that current. Equivalently, for a source that supplies a fixed amount of power, the addition of a reactive component reduces the current that can be drawn by the circuit.

It is desirable for the prototype to provide high current to the coils with low power input. The presence of reactive power in the circuit is an obstacle to these goals. However, the effect of reactive power can be mitigated by correcting the power factor of the circuit. Capacitors have reactance values that are opposite in sign to the reactance values of inductors. Adding an appropriately sized capacitor to an inductive circuit will cause the reactance of the capacitor to cancel out the reactance of the inductor. This reduces the net reactance of the load of the circuit, which reduces the reactive power seen by the source.

If the capacitor is matched so that the net reactance of the load becomes zero, the reactive power seen at the source is completely eliminated, and the power factor of the circuit is 1. When

the matching capacitor is connected in series to the inductor, the LC pair will act like a short to the rest of the circuit. Correcting the power factor to unity also causes the circuit to become resonant. This causes the voltages across the capacitor and inductor individually to have much higher amplitude than the source. However, the capacitor voltage is 180° out of phase with the inductor voltage while being the same magnitude, so they destructively interfere. Because of this, these high voltages are not seen by the rest of the circuit. This is an important consideration when selecting a correction capacitor, because that capacitor must be rated to handle very high voltage.

To correct the power factor to unity, the reactance of the capacitor must have the same magnitude as the reactance of the inductive component. Thus, to determine an appropriate correction capacitor, the reactance of the RMF coils must be known. To determine the reactance of an inductive component, it can be connected in series to a resistor and supplied with a sinusoidal AC source. The circuit diagram of this configuration is shown in Figure 4.8.

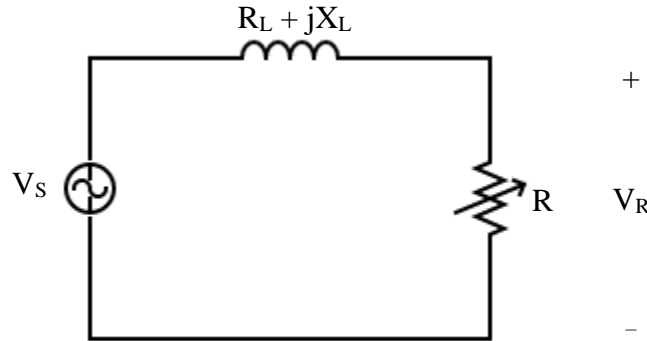


Figure 4.8 – Reactance testing circuit diagram.

The resistance of the resistor R is varied until it reaches a value where the amplitude of the voltage across the resistor is half of the amplitude of the source voltage. When this condition is met, phasor circuit analysis can be used to find the expression for the reactance of the inductor given by Eq. (4.2).

$$X_L = \sqrt{3R^2 - 2R_L R - R_L^2} \quad (4.2)$$

The derivation of Eq. (4.2) is given in Appendix A. The results of this reactance testing procedure for the RMF coils are discussed in Section 4.4.2.

4.4 Test Results and Discussion

4.4.1 Signal Generation Testing

The signal generator circuit described in Section 4.2 was tested by measuring the output voltages of the phase splitter network with an oscilloscope. An image of the oscilloscope output when comparing both outputs simultaneously is shown in Figure 4.9.

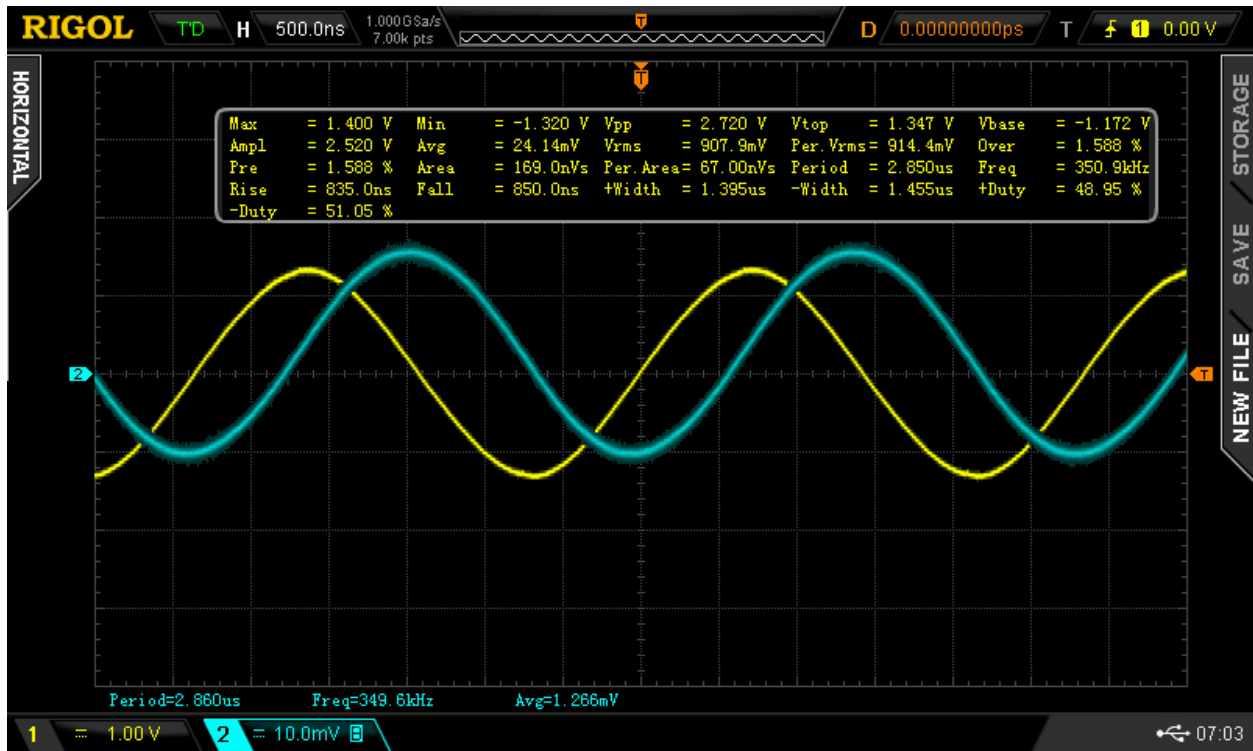


Figure 4.9 – Oscilloscope measurement of both phase splitter outputs.

It can be seen from this oscilloscope reading that the outputs have a phase difference of approximately 90° . This means that the phase splitter network was able to perform its predicted function. Additionally, the frequency of both outputs is approximately 350 kHz. This means that the frequency tuning resistors and capacitors in the XR2206 circuit were sized appropriately.

It should be noted that the probe connected to channel 2 of the oscilloscope was malfunctioning. It was able to correctly measure the frequency and phase of the signal, but the amplitude was incorrect. To accurately measure the amplitude of both outputs, each output was measured individually with the functional oscilloscope probe. The oscilloscope readings of these individual measurements are shown in Figure 4.10 and Figure 4.11.

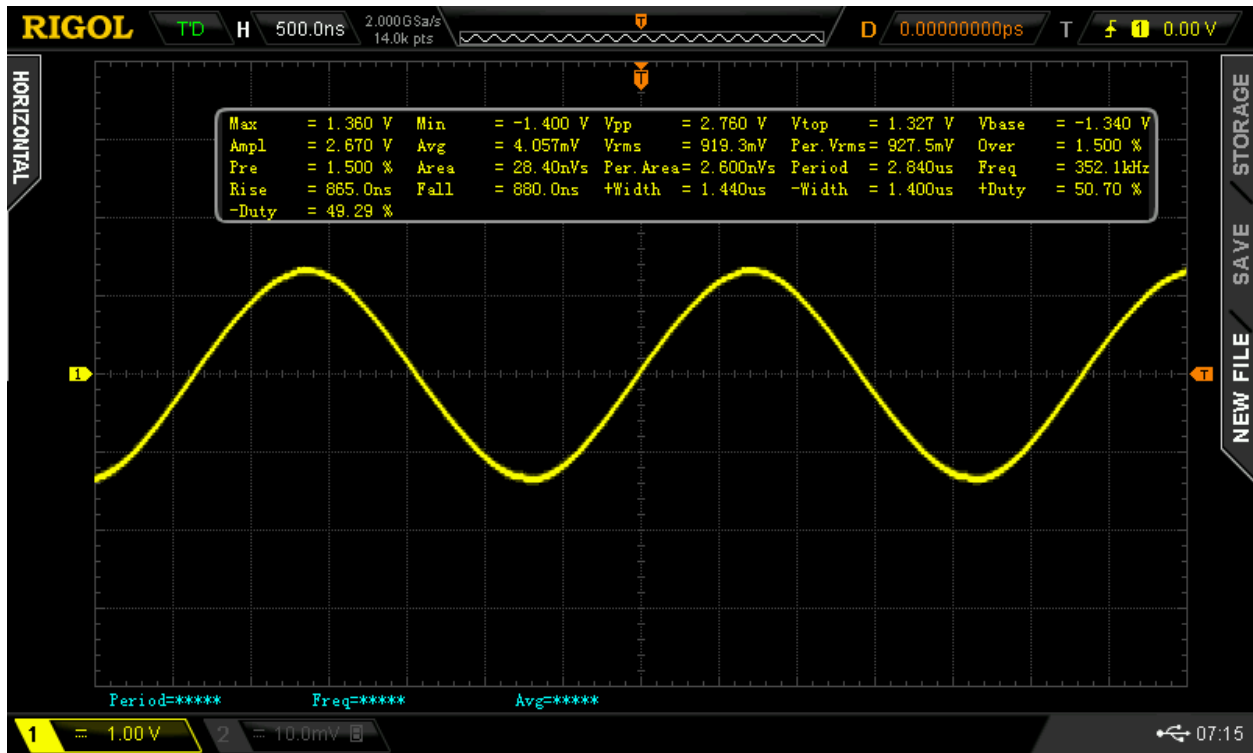


Figure 4.10 – Oscilloscope measurement of output 1 of the phase splitter.

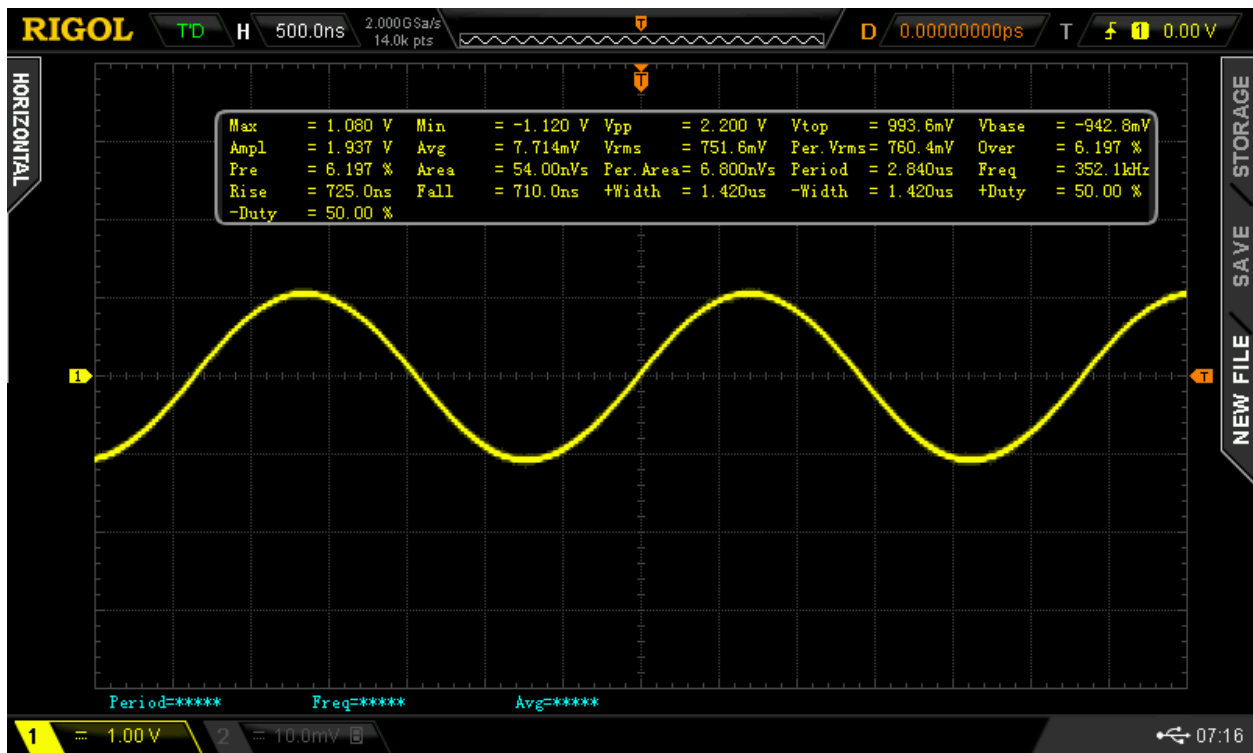


Figure 4.11 – Oscilloscope measurement of output 2 of the phase splitter.

It can be seen from the individual measurements that both outputs are sinusoidal, with minimal visible distortion. This means that the XR2206 circuit was adequately configured to produce a minimally distorted sinusoidal waveform. Additionally, both output waveforms are nearly centered around the 0 V line. This means that the high pass filter was adequately able to remove the DC bias from the output signal. Finally, the amplitude of output 1 is approximately 1.38 V, while the amplitude of output 2 is approximately 1.1 V. These values differ from each other by approximately 22.6%. This difference in amplitude is likely due to the pole frequency of the phase splitter network not matching the signal frequency exactly. This was likely caused by variations in actual resistance and capacitance values due to component tolerance ranges. This amplitude difference could potentially be corrected by using additional resistors in the phase splitter circuit to achieve the desired resistance values more precisely.

4.4.2 Coil Reactance Testing

The reactance of the RMF coils was calculated using the procedure described in Section 4.3. To do this, a single pair of the RMF coils was connected in series to the signal generator circuit described in Section 4.2, and to a potentiometer configured as a variable resistor. This circuit was configured to match the diagram shown in Figure 4.8. The output of the high pass filter in the signal generator circuit was used as the voltage source for this test; the outputs of the phase splitter were not used because phase shifted signals were not necessary for the test.

The source voltage amplitude was measured with an oscilloscope to be 1.5 V. The resistance of the potentiometer was then adjusted until the amplitude of the voltage across the potentiometer was measured to be 750 mV. When this condition was reached, the resistance of the potentiometer was measured to be 138 Ω . The DC resistance of the coil pair was measured to be 0.2 Ω . These values were inserted into Eq. (4.2) to calculate the coil pair reactance. The reactance of the single RMF coil pair was calculated to be 239 Ω .

The reactance of an inductor is related to its inductance by Eq. (4.3).

$$X_L = \omega L \quad (4.3)$$

Since the signal frequency is known, and the reactance of the coil pair has been calculated, Eq. (4.3) can be used to calculate the inductance of the coil pair. The coil pair inductance was calculated to be 0.11 mH using this equation. The inductance of the coils is a useful parameter for comparing simulation results to physical test results, so it is worthwhile to calculate.

The capacitance of an appropriate power factor correction capacitor can be calculated through Eq. (4.4).

$$|X_L| = |X_C| = \frac{1}{\omega C} \quad (4.4)$$

A correction capacitance value for the RMF coil pair was calculated to be 1.9 nF. An LTspice simulation was made of the RMF coil pair and correction capacitor. These components were connected in series. In this simulation, the LC pair was supplied power by an amplifier circuit with output current and voltage values similar to what might be used in the physical prototype. The current supplied by the amplifier had an amplitude of approximately 2 A, and the voltage

supplied by the amplifier had an amplitude of approximately 6 V. In this simulation, the voltage across the capacitor had an amplitude of approximately 450 V. The capacitor voltage being much higher than the source voltage was expected due to the resonance of the corrected circuit, as discussed in Section 4.3. This voltage will be used as a lower bound for the voltage rating when selecting an appropriate physical correction capacitor.

5 Prototype Design – Axial Coil and Power Systems

5.1 Introduction

The next phase of the prototype design was to construct all the remaining components that required electrical power input. Since the RMF signal generator was already constructed as described in Chapter 4, the remaining system components that require electrical power were the axial coil and the RMF signal amplifier. After these components were constructed, the total electrical power input required for the coil array system was able to be measured. This measured system input power was then compared to the system input power requirement that was set in Chapter 1.

5.2 Axial Coil Design

As discussed in Chapter 1, the main function of the axial coil in a rotating magnetic field thruster is to produce a steady axial magnetic field with a radial component. Because the magnetic field generated by the axial coil is steady, the coil can be powered directly by a DC source. Because of this, the only design consideration for the axial coil system is the winding of the coil itself.

As discussed at the end of Chapter 3, the axial coil design chosen for the prototype consists of a single coil that expands outward along its length. To achieve this shape, the coil was wound around a scaffold structure in the shape of a cone section. This scaffold structure was additively manufactured from PLA plastic using an FFF 3D printer. The narrow end of the cone section had a diameter of 8 cm, and the wide end had a diameter of 9.2 cm. The length of the cone section was 5.6 cm. To maintain the position of the wire during coil winding, a helical channel was added to the surface of the cone section. This channel had 10 turns, which was the turn count chosen for the coil. The channel diameter was 0.15 cm, which was chosen to accommodate the wire size used for the coil. A schematic diagram of the CAD model used for 3D printing the scaffold is shown in Figure 5.1. An image of the 3D printed scaffold is shown in Figure 5.2.

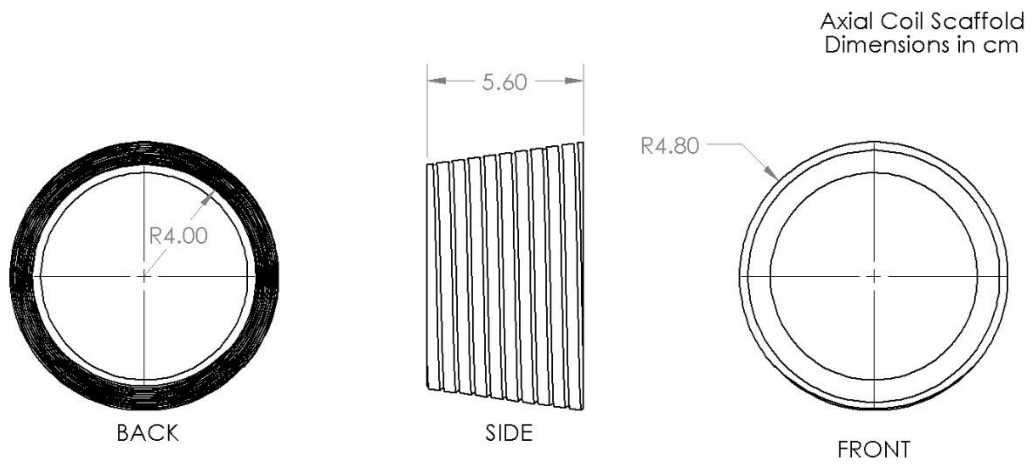


Figure 5.1 – Schematic diagram of the axial coil scaffold.



Figure 5.2 – 3D printed axial coil scaffold.

The coil was wound using the same type of 16 AWG enameled copper magnet wire that was used in the RMF coils. After the coil was wound, ribs of nonconductive adhesive tape were added along its length to prevent the coil from expanding out of its shape. The scaffold structure was then removed from the coil. The scaffold was removed in this case because the axial coil is a single contiguous piece; the RMF coils included their scaffold as part of the permanent structure because there were two separate coils that needed to be kept in alignment. An image of the wound axial coil is shown in Figure 5.3.

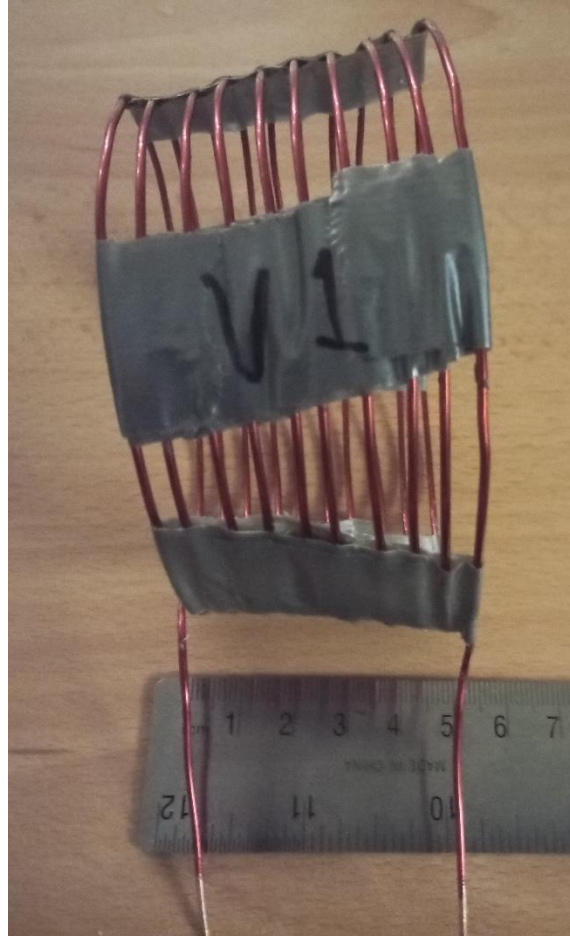


Figure 5.3 – Axial coil winding.

Since the axial coil only requires DC input, it was powered using a benchtop DC power supply. The current supplied to the axial coil was able to be directly set using the interface of the DC power supply. It is desirable to have a known relationship between the axial coil current and RMF coil current, since current determines magnetic field strength. To facilitate this, a value for the axial coil current was not chosen until after the RMF amplifier output current was determined. The current supplied to the RMF coils is much more difficult to vary because it depends on the output of an amplifier, so it is more feasible to match the axial coil current to it. For the purposes of testing this prototype, the axial coil current will be chosen to be equal in magnitude to the RMF coil current. However, other relationships would be considered in future work involving plasma testing. The design and testing of the RMF amplifier is discussed in Section 5.3, and the value of the axial coil current chosen based on those results is discussed in Section 5.4.

5.3 RMF Amplifier Design

The main electrical parameter in magnetic field generation is current; increasing current through a coil will increase the strength of the generated magnetic field. Because of this, it is desirable to have high current through the coils in this coil array. As discussed in Section 5.2, the axial coil uses a DC source, so the current through the coil can be set as desired within the limits

of the power supply. However, the RMF coils use an AC source, and this source has an output signal that is not easily variable. An amplifier was thus needed to increase the current through the RMF coils. The main criteria for this amplifier were that it should substantially increase the current in the RMF coils without distorting the signal waveform. A range of 1-6 A was selected for the desired output current target.

There were two main difficulties in choosing an amplifier circuit for this project. The first was that most discrete transistor amplifier circuits are designed for either audio or radio frequency ranges. The RMF frequency of 350 kHz used in this project is not well suited to either of these ranges; it is higher than typical audio frequencies and uncommon in modern radio applications. Because of this, it was considered unlikely that amplifiers for these frequency ranges would be suitable for this project. The second difficulty involved amplifier circuits based on operational amplifier ICs. Many op-amps are not suitable for a frequency of 350 kHz, and most op-amps have output current in the mA range.

An amplifier IC that was determined to be suitable for this project was the LT1210. This IC has frequency response parameters that make it capable of reproducing a 350 kHz signal without distortion. Additionally, the LT1210 has a maximum output current of 2 A, which is within the target range. A current amplifier circuit obtained from the LT1210 datasheet was chosen as the amplifier circuit for this project. A diagram of this circuit is shown in Figure 5.4 [26].

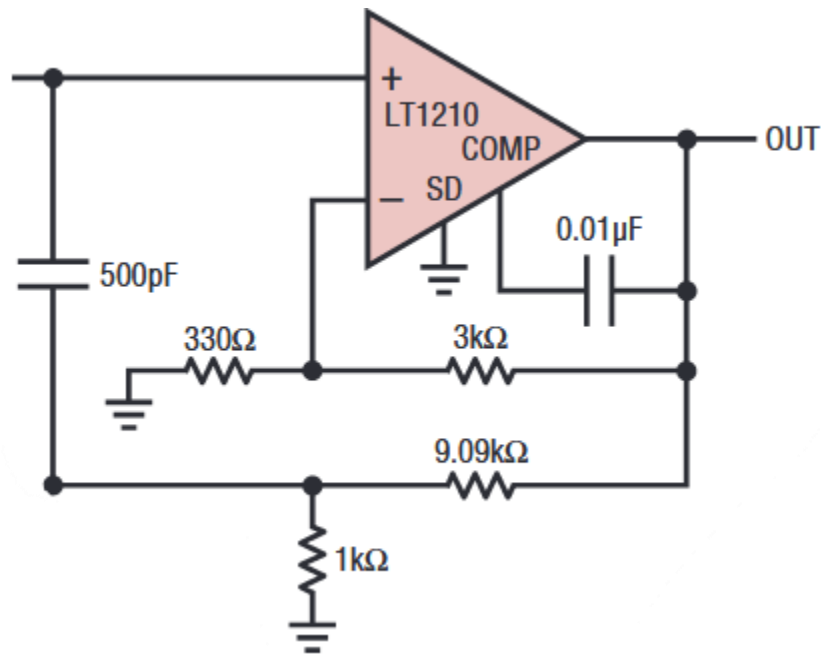


Figure 5.4 – Amplifier circuit diagram from the LT1210 datasheet [26].

The circuit in Figure 5.4 was constructed as depicted, with the only modification being the addition of 1 μ F bypass capacitors connected to the power supply pins. Because there were two signal channels that required amplification, two copies of the circuit were constructed. The positive supply pins, negative supply pins, and ground points of these circuits were connected in parallel to the power supply. These circuits were supplied by a dual power source that consisted

of two channels of a DC power supply connected in series. Heat sinks were attached to the LT1210 ICs as it was expected that the ICs might potentially dissipate significant amounts of power. An image of the assembled amplifier circuit board is shown in Figure 5.5.

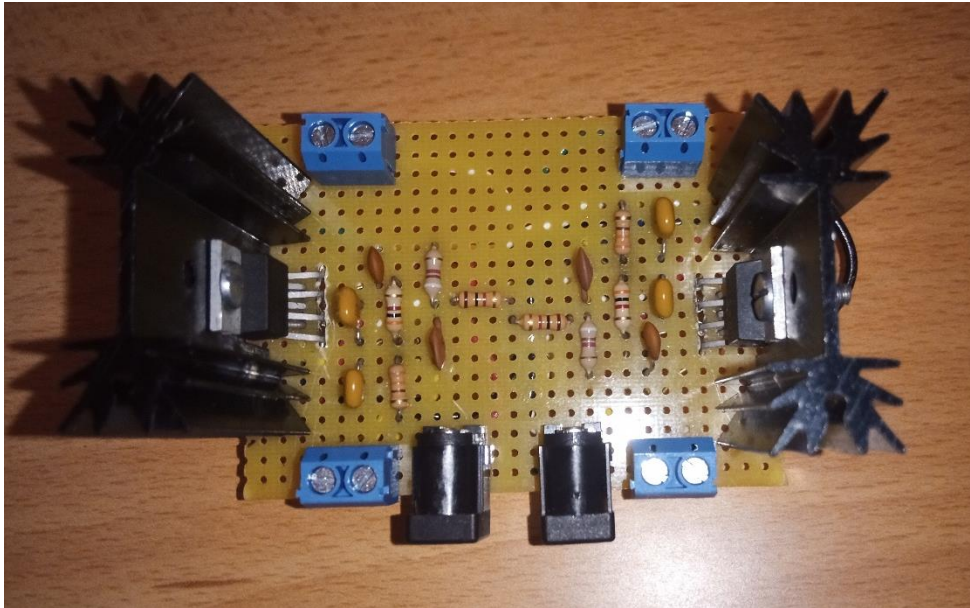


Figure 5.5 – Assembled RMF amplifier circuit.

Each output of the amplifier circuit was connected to a series RLC network. This network consisted of:

- a 10 W rated 5 Ω resistor parallel pair
- one pair of the RMF coils
- a correction capacitor array with an equivalent capacitance of 1.9 nF

An additional test was performed with the amplifier circuit connected to the RMF coils and the parallel resistor pair, without the correction capacitor array. In each test, the voltage amplitude was measured across the resistor pair, and across the entire load, in both the output branches of the circuit. The voltage across the resistor pair was used to calculate the current amplitude using the phasor form of Ohm's law shown in Eq. (5.1).

$$|\tilde{i}| = \frac{|\tilde{v}|}{|Z|} \quad (5.1)$$

This current was possible to calculate because the parallel resistor pair had a known, measured resistance of 2.5 Ω . Since the load elements were connected in series, the current through the resistor could be considered the current through the entire load. The measured voltage values and calculated current values in both the output branches of the circuit are shown in Table 5.1.

Table 5.1 – Amplifier circuit output measurements.

Test case	Total load voltage amplitude	Resistor voltage amplitude	Calculated current amplitude
RLC load, horizontal coil branch	4.8 V	0.060 V	0.024 A
RLC load, vertical coil branch	5.7 V	0.072 V	0.029 A
RL load, horizontal coil branch	3.4 V	0.64 V	0.25 A
RL load, vertical coil branch	4.8 V	0.81 V	0.32 A

As seen in Table 5.1, the current through the RLC network is much lower than the maximum possible output current of 2 A. The current output of this amplifier circuit varies significantly with the load impedance, which suggests that the impedance of the RLC network is much higher than expected. This high impedance is most likely due to the capacitor reactance not matching the coil reactance. This discrepancy was likely caused by an error in the voltage measurement procedure when performing the reactance measurement tests described in Chapter 4.

To test if an error was made in the initial measurement of the RMF coil reactance, the load reactance magnitude was calculated for each test case of the amplifier output. Reactance values were calculated using Eq. (5.2), which was obtained by expanding the impedance magnitude in Eq. (5.1) and solving for reactance.

$$X = \sqrt{\left(\frac{|\tilde{V}_S|}{|I|}\right)^2 - R^2} \quad (5.2)$$

The values of current and voltage used in Eq. (5.2) were obtained from Table 5.1. The calculated load reactance for each test case is shown in Table 5.2.

Table 5.2 – Calculated load reactance values.

Test case	Load reactance magnitude
RLC load, horizontal coil branch	200 Ω
RLC load, vertical coil branch	198 Ω
RL load, horizontal coil branch	13 Ω
RL load, vertical coil branch	14 Ω

In the RL test case, the only source of reactance is the RMF coil pair. The measured reactance values in Table 5.2 suggest that the coil pairs have reactance values of 13-14 Ω , which supports the idea that there was an error in the initial reactance measurement. The values in Table 5.2 also support the idea that the impedance of the RLC case is much higher than expected. The calculated load reactance in the RLC case was approximately 200 Ω . If the coil

reactance is on the order of 10 Ω , then it is reasonable for the LC pair reactance to be on the order of 200 Ω , since the capacitor array was sized to have a reactance of 239 Ω .

Since the capacitor network was not properly sized to match the coil reactance, the coils were connected directly to the amplifier output without the capacitors. The voltage across the coils was measured, and the current through the coils was calculated using the reactance values in Table 5.2. The voltage and current values for each coil pair are shown in Table 5.3.

Table 5.3 – Amplifier circuit output measurements for coil-only load.

Component	Measured voltage amplitude	Calculated current amplitude
Horizontal coil	3.3 V	0.251 A
Vertical coil	4.3 V	0.298 A

Based on the values in Table 5.3, the current through the coils in this case was in the range of 0.25-0.3 A. These values are still lower than desired, but they were larger than the other tested cases, and they were thought to be sufficient for generating a measurable magnetic field.

5.4 System Power Input Measurement

All of the electrical systems in the prototype are supplied by DC sources. This means that the supplied power for each circuit can be calculated directly as the product of the supply current and supply voltage. Additionally, the benchtop power supplies used in this project measure the current, voltage, and power supplied to each output channel. The readings from each power supply channel used in the prototype are shown in Table 5.4.

Table 5.4 – Power supply channel measurements of prototype electrical systems.

Power supply channel	Supply voltage	Supply current	Supplied power
RMF signal generator supply	12.846 V	0.017 A	0.218 W
RMF amplifier positive supply	15.009 V	0.256 A	3.842 W
RMF amplifier negative supply	14.995 V	0.214 A	3.209 W
Axial coil supply	0.202 V	1.999 A	0.404 W

The total electrical power supplied to the prototype was calculated to be 7.673 W. This value is much lower than the requirement threshold of 1kW. However, this large difference is to be expected because the current values used in this project are much lower than would typically be used for even a small scale RMF thruster. Based on this result, the current, and thus the magnetic field strength, could be increased significantly in future work without exceeding the requirement threshold.

In this setup, the axial coil was set to have a current of 2 A. As discussed in Section 5.3, the current output of the amplifier circuit was lower than desired. However, the maximum current output of the LT1210 is 2 A, so 2 A can be considered the upper bound of the axial coil current

when it is matched to the RMF current. The axial coil supply parameters were measured at this upper bound to determine the maximum power input to the axial coils possible in this prototype configuration.

6 Magnetic Field Measurement and Simulation Environment Validation

6.1 Introduction

The final stage of the project was to measure the magnetic field generated by the prototype and compare it to data obtained from simulations. The goal of this comparison was to validate the results of the simulation environment with experimental data. If the simulation environment is validated, then it could be used to study the magnetic fields generated by other coil configurations without needing to construct additional coil prototypes. It should be noted that this comparison process was only intended to validate the vacuum magnetic field data from the simulation environment. Validating any plasma behavior in the simulation environment would require an experiment that involves physically generating plasma, which is beyond the scope of this project.

6.2 Magnetic Field Measurement

As discussed in Chapter 1, the prototype was originally intended to be tested in a vacuum chamber. This was to avoid accidentally forming plasma from the surrounding air, which would both be potentially hazardous and affect the magnetic fields generated by the coils. However, based on the testing performed in Chapter 5, it was determined that the power input to the RMF coils was too low to generate plasma. Because of this, the prototype was able to be tested without a vacuum chamber, since air in its normal state does not significantly affect magnetic fields.

The coil array was assembled with wooden support posts attached to the axial and RMF coil structures. The posts were fastened into a base and aligned so that the axial coil was centered around the RMF coil structure. An image of the assembled coil array is shown in Figure 6.1.

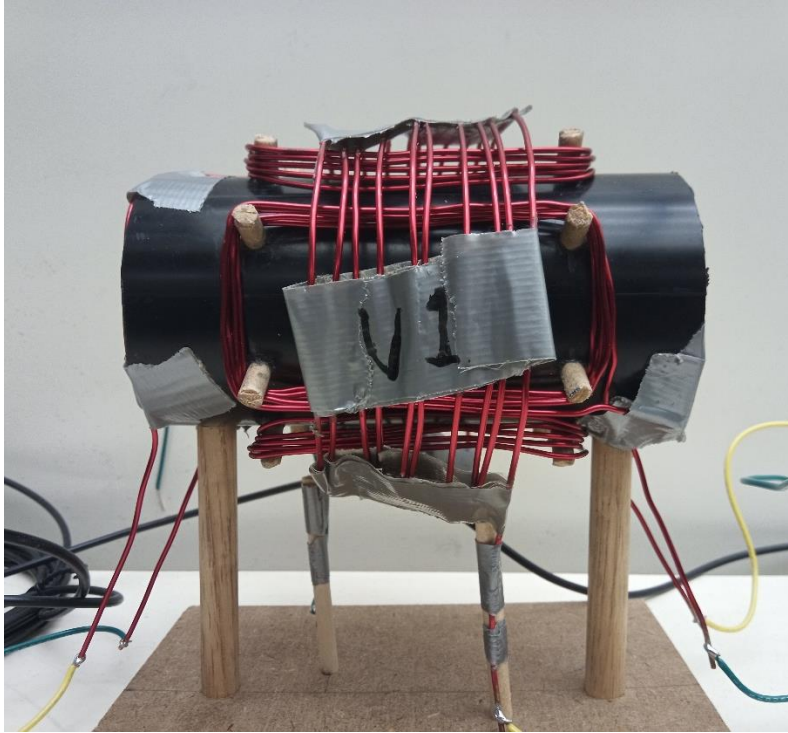


Figure 6.1 – Fully assembled coil array.

The magnetic field of the coil array was measured with a Hall effect sensor. The sensor was only able to detect a magnetic field on a single axis. Since the rotating and axial magnetic fields are orthogonal to each other, they were measured in separate tests. The rotating magnetic field was measured with the sensor axis aligned vertically, and the axial magnetic field was measured with the sensor axis aligned with the axis of the axial coil. For all tests, the sensor was placed inside the scaffold tube of the RMF coils, at the center point.

The output voltage of the Hall effect sensor was measured with an oscilloscope, and the voltage data were converted to magnetic field values using properties from the sensor datasheet. The sensor used in this project has a linear voltage response to magnetic fields. A graph of the B-V response function was obtained from the sensor datasheet and is shown in Figure 6.2 [27].

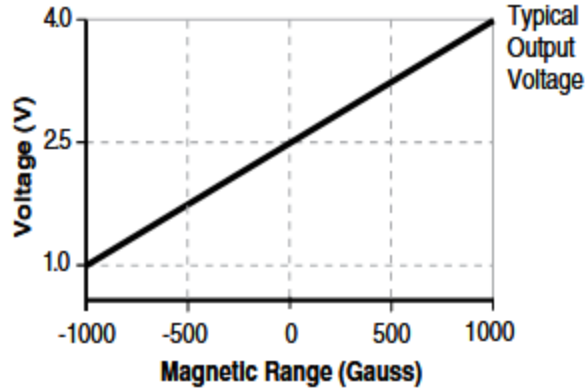


Figure 6.2 – Hall effect sensor magnetic field-voltage response curve [27].

Based on the graph in Figure 6.2, the Hall effect sensor has a voltage response given by the function in Eq. (6.1).

$$V = sB + V_c \quad (6.1)$$

The value V_c is the voltage output when the sensor is detecting no magnetic field. From the datasheet, this zero-point value is approximately half the supply voltage. When the sensor was powered with a supply voltage of 5 V, the zero-point voltage was measured to be 2.565 V. The value s is the sensitivity of the sensor. From the datasheet, the sensitivity is 1.4 mV/G, or 14 V/T. Eq. (6.1) can be rearranged to calculate the detected magnetic field strength for any given output voltage of the sensor. This equation is shown in Eq. (6.2).

$$B = \frac{V - V_c}{s} \quad (6.2)$$

The measured sensor output voltage and calculated magnetic field strength data are discussed in Section 6.4.

6.3 Simulation Environment Validation

The coil array was modeled in STAR-CCM+ to compare measured results to simulation results. The dimensions of the coil array model were chosen based on physical measurements of the coil array prototype. An image of the coil array geometry in the simulation is shown in Figure 6.3.

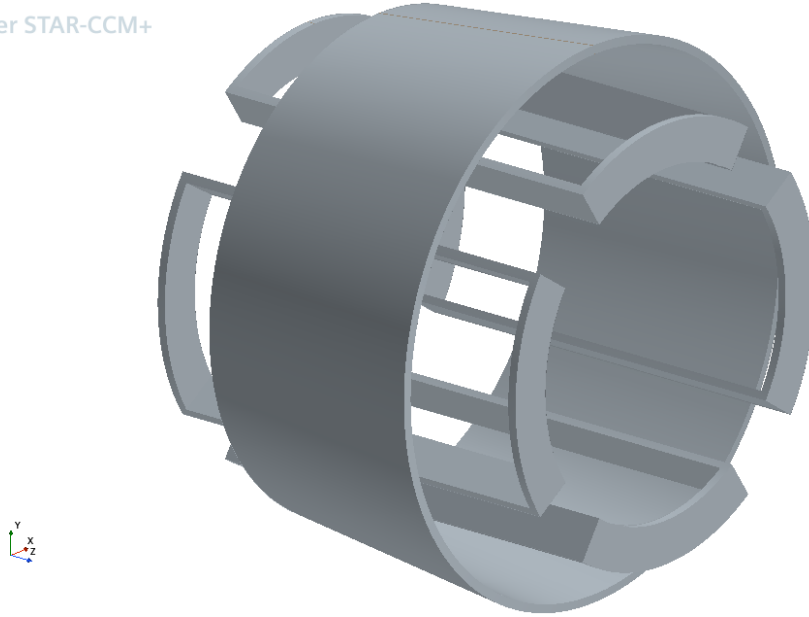


Figure 6.3 – Simulated geometry of the coil array prototype.

The coil array, and the region of vacuum surrounding it, were discretized with a polyhedral mesh. This mesh had an element count of approximately 2.1 million. An image of a cross-section of the mesh orthogonal to the coil array axis is shown in Figure 6.4.

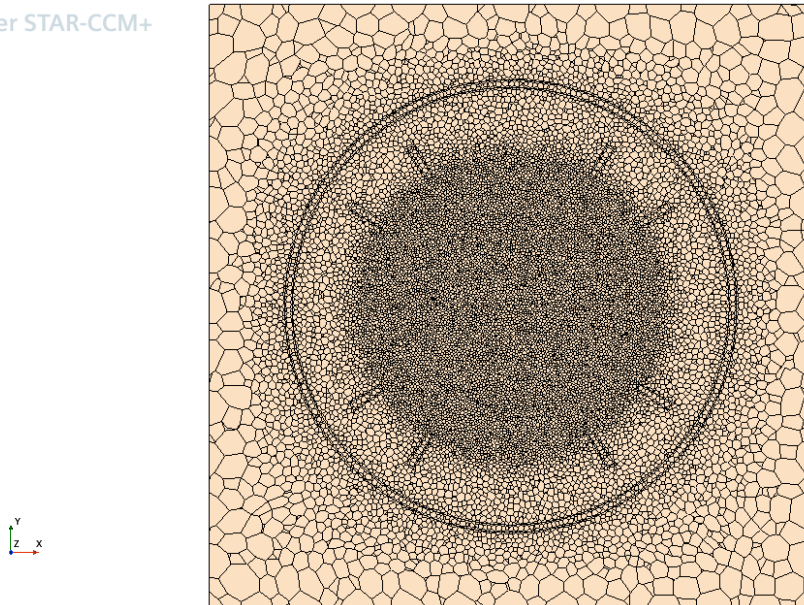


Figure 6.4 – Cross section of the prototype simulation mesh in the x-y plane.

Since no fluid was modeled in this simulation, only electromagnetic models were used. Since the magnetic field tests measured the effects of the rotating and axial magnetic fields separately, two separate simulation cases were run. The first case was a transient simulation of the rotating magnetic field. The RMF coils were given sinusoidal currents with amplitude values taken from

Table 5.3 and a frequency of 350 kHz, and the axial coil was left inactive. The second case was a steady state simulation of the axial magnetic field. The axial coil was given the current value of the axial coil power supply in Table 5.4, and the RMF coils were left inactive.

Magnetic field strength was measured on each coordinate axis of the simulation. The total magnitude of the magnetic field strength was also measured. For the RMF case, data for the y-axis component of the magnetic field was collected, because the y-axis in the simulation corresponded to the vertical axis of the prototype. For the axial case, data for the z-axis component of the magnetic field was collected because the z-axis in the simulation corresponded to the axial coil axis in the prototype. The results of the simulation cases are discussed in Section 6.4.

6.4 Results and Discussion

6.4.1 Rotating Magnetic Field Comparison

Oscilloscope measurements of the Hall effect sensor output voltage from the RMF measurement test were recorded as discussed in Section 6.2. A plot of the recorded voltage data is shown in Figure 6.5. The recorded waveform is sinusoidal, which is the expected behavior of a single component of a rotating vector.

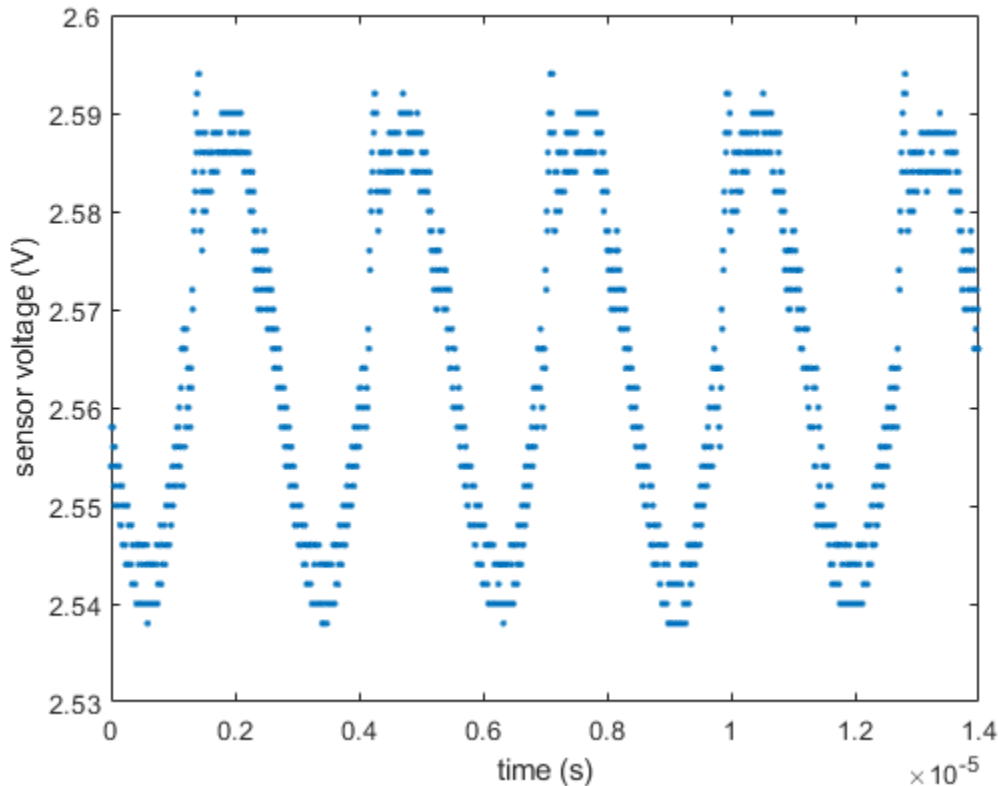


Figure 6.5 – Measured Hall effect sensor output voltage for the RMF test.

The recorded voltage data were converted to magnetic field strength values using Eq. (6.2). A plot of the magnetic field strength data is shown in Figure 6.6. The shape of the waveform is

the same as the voltage data but is now centered around a magnitude of zero, which is the expected outcome of using Eq. (6.2). The amplitude of this magnetic field data is 1.9 mT.

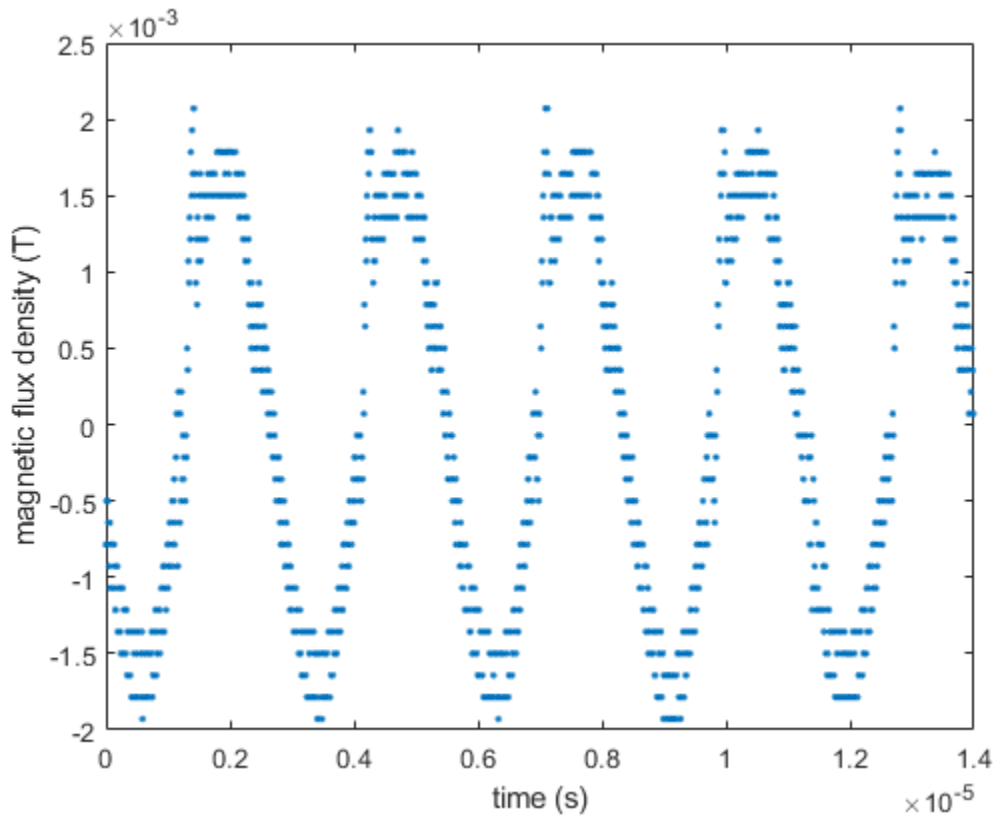


Figure 6.6 – Measured magnetic field strength of the rotating magnetic field y-component.

Data of the y-axis component of the magnetic field strength was collected from the RMF simulation case as discussed in Section 6.3. A plot of this data is shown in Figure 6.7. The waveform is sinusoidal, and the frequency is nearly identical to the measured waveform. However, the amplitude of the simulated magnetic field data is 0.016 mT, which is approximately two orders of magnitude lower than the measured waveform amplitude. A plot comparing the simulated data to the measured data is shown in Figure 6.8.

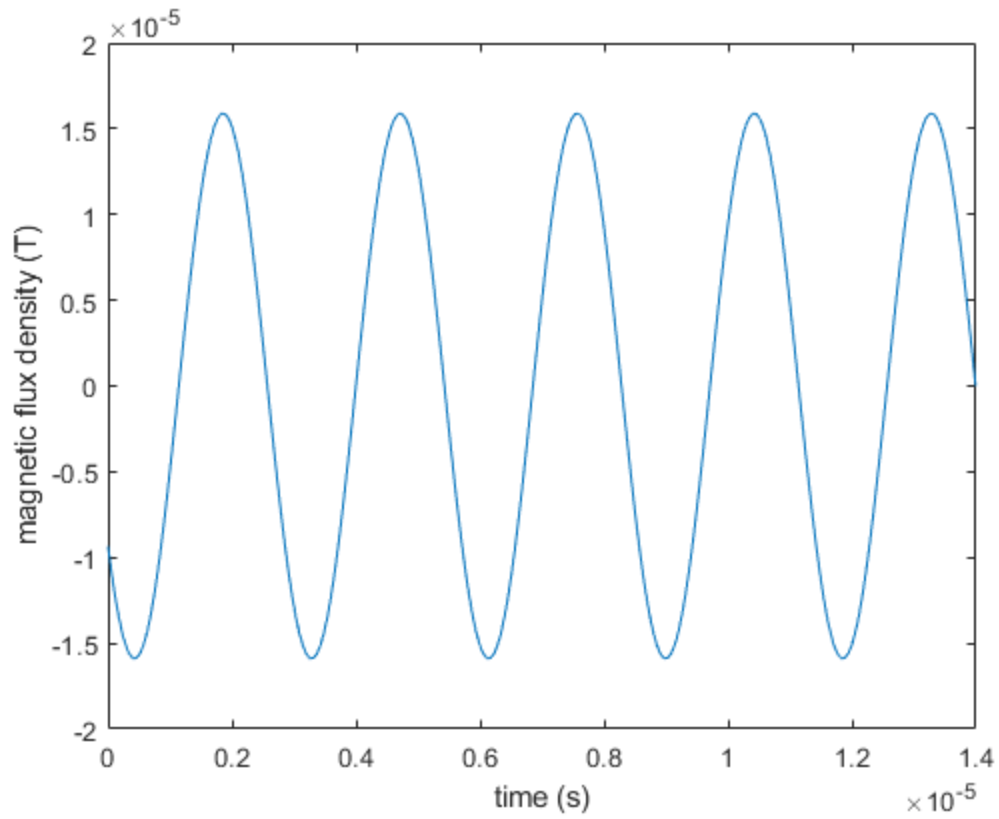


Figure 6.7 – Simulated magnetic field strength of the rotating magnetic field y-component.

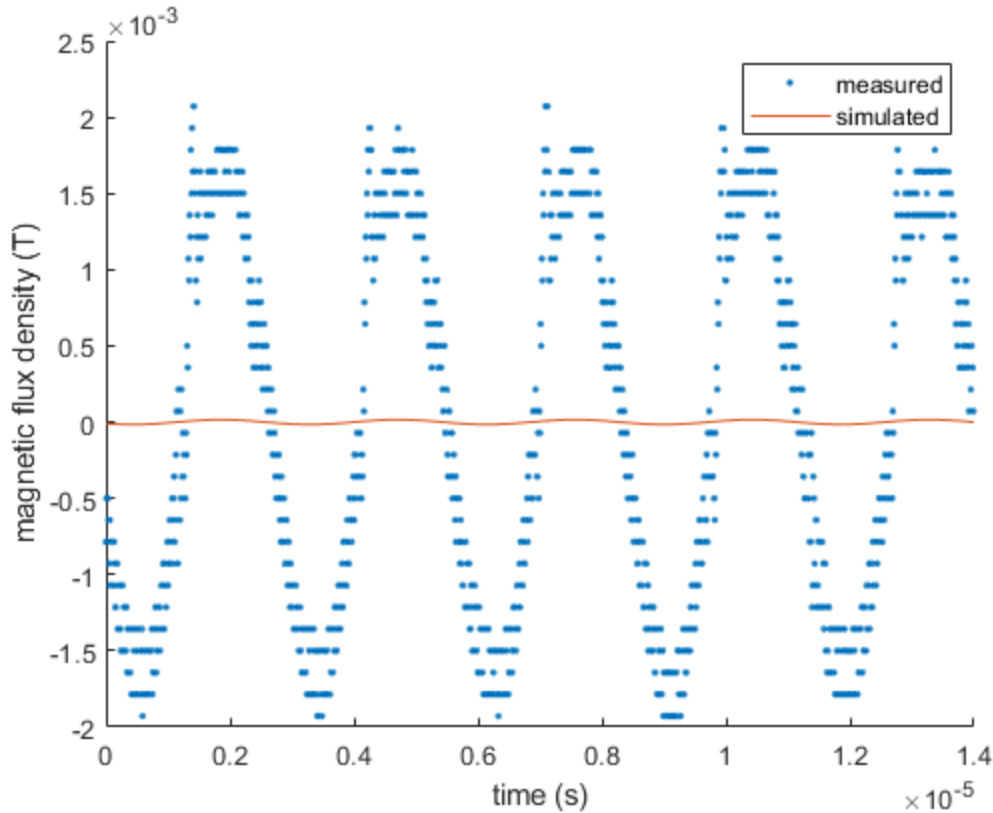


Figure 6.8 – Comparison between measured and simulated RMF strength.

There are many potential causes for this discrepancy. One potential cause is that the magnetic field may have induced additional voltage in the wires connected to the Hall effect sensor. If that occurred, then the voltage recorded by the oscilloscope would have been higher than what the sensor would have otherwise output. Another potential cause is that the current in the RMF coils may have been higher than what was calculated in Chapter 5. If the current in the coils were higher than these values, then the simulation, which used those values, would give incorrect results. A third potential cause is that there may have been an as-yet unknown error made in setting up the simulation environment.

The potential cause of higher-than-expected current was able to be tested using the simulation environment. An additional simulation case was made where the RMF coils were given a current amplitude of 2 A. Since the amplifier used in the prototype has a maximum output of 2 A, this can be considered the upper bound for the current amplitude in the prototype. The magnetic field strength in this simulation case had an amplitude of 0.11 mT, which is still an order of magnitude lower than the measured data. Because of this, the coils having higher current than calculated was ruled out of being the sole cause of the discrepancy shown in Figure 6.8.

6.4.2 Axial Magnetic Field Comparison

The Hall effect sensor output voltage for the axial magnetic field measurement test was recorded as described in Section 6.2. In this test, the Hall effect sensor had a constant output voltage of 3 mV. This value was inserted into Eq. (6.2), and the calculated magnetic field

strength was 0.21 mT. Data of the z-axis component of the magnetic field strength was collected from the axial simulation case as discussed in Section 6.3. The z-axis component of the simulated magnetic field strength had a constant value of 0.18 mT. The simulated value differs from the measured value by approximately 16%. This difference could be accounted for by the tolerance in the Hall effect sensor sensitivity. When accounting for the full sensitivity range specified by the datasheet [27], the measured magnetic field strength would be within the range of 0.17-0.3 mT, and the value from the simulation is in this range. These values are much closer to agreement than the data for the RMF case. The only difference in the simulation environment between the axial and RMF cases was the use of a steady state solver rather than a transient one. Because of this, an unknown error in the simulation environment can be ruled out as the cause of the discrepancy discussed in Section 6.4.1.

The comparison of the axial magnetic field data suggests that the simulation environment is reasonably able to simulate the vacuum magnetic fields of electromagnetic coils. However, more testing of the rotating magnetic field should be done to investigate the cause of the discrepancy in that case. In these tests extra precautions would need to be taken to prevent the wires connected to the sensors from interfering with the results.

7 Conclusion and Suggestions for Future Work

The goal of this project was to develop a coil array for use in an RMF plasma thruster. The work performed for this project was intended to act as the first step in an iterative process for the development of this coil array. Based on the results of the prototype testing, it can be reasonably concluded that the simulation environment was validated for vacuum magnetic field simulations.

A proposed next step in this process would be to use the simulation environment to further explore how variations in coil shape and current affect the topology and strength of the generated magnetic field. Theory on FRC plasma behavior could then be used to analyze these simulation results and determine coil parameters suitable for FRC formation. The prototype could then be modified to achieve the magnetic field determined from these simulations. The prototype was designed to be modular so that components could be individually replaced in anticipation of such future modifications. After these modifications are made, plasma formation testing of the prototype could be performed, and the results of this testing could be used to validate the plasma behavior of the simulation environment. Once that validation is performed, the simulation environment could be more confidently used to determine performance parameters of further iterations of thruster designs.

8 References

- [1] Charles, C. “Plasmas for Spacecraft Propulsion.” *Journal of Physics D: Applied Physics*, Vol. 42, No. 16, 2009, p. 163001. <https://doi.org/10.1088/0022-3727/42/16/163001>.
- [2] Bathgate, S. N., Bilek, M. M. M., and McKenzie, D. R. “Electrodeless Plasma Thrusters for Spacecraft: A Review.” *Plasma Science and Technology*, Vol. 19, No. 8, 2017, p. 083001. <https://doi.org/10.1088/2058-6272/aa71fe>.
- [3] Sun, Y., Levchenko, I., Lim, J. W. M., Xu, L., Huang, S., Zhang, Z., Thio, F., Potrivitu, G.-C., Rohaizat, M. W. A. B., Cherkun, O., Chan, C. S., Baranov, O., Bazaka, K., and Xu, S. “Miniaturized Rotating Magnetic Field–Driven Plasma System: Proof-of-Concept Experiments.” *Plasma Sources Science and Technology*, Vol. 30, No. 6, 2021, p. 065003. <https://doi.org/10.1088/1361-6595/ab9b34>.
- [4] Arefiev, A. V., and Breizman, B. N. “Theoretical Components of the VASIMR Plasma Propulsion Concept.” *Physics of Plasmas*, Vol. 11, No. 5, 2004, pp. 2942–2949. <https://doi.org/10.1063/1.1666328>.
- [5] Díaz, F., Squire, J., Ilin, A., Mccaskill, G., Nguyen, T.-X., Winter, D., Petro, A., Goebel, G., Cassady, L., Stokke, K., Dexter, C., Graves, T., Jr, L., George, J., Bengtson, R., Breizman, B., Jacobson, V., Arefiev, A., Chan, A., and Glover, T. The Development of VASIMR Engine. In *Proceedings of International Conference on Electromagnetics in Advanced Applications (ICEAA99)*, No. 37831, Torino, Italy, 1999, pp. 99–102.
- [6] Chang Diaz, F. R., Giambusso, M., Corrigan, A. M. H., Dean, L. O., and Warrayat, M. F. Recent Progress on the VASIMR Engine. Presented at the 37th International Electric Propulsion Conference, Cambridge, Massachusetts, U.S.A., 2022.
- [7] Charles, C., and Boswell, R. “Current-Free Double-Layer Formation in a High-Density Helicon Discharge.” *Applied Physics Letters*, Vol. 82, No. 9, 2003, pp. 1356–1358. <https://doi.org/10.1063/1.1557319>.
- [8] Charles, C., Alexander, P., Costa, C., Sutherland, O., Boswell, R., Pfitzner, L., Franzen, R., Kingwell, J., Parfitt, A., Frigot, P.-E., Gonzalez del Amo, J., and Gengembre, E. “Helicon Double Layer Thrusters.” *Collection of Technical Papers - AIAA/ASME/SAE/ASEE 42nd Joint Propulsion Conference*, Vol. 7, 2006. <https://doi.org/10.2514/6.2006-4838>.
- [9] Harle, T., Pottinger, S. J., Lappas, V. J., Charles, C., Boswell, R. W., and Perren, M. Thrust Measurements of a Small Scale Helicon Double Layer Thruster. Presented at the 32nd International Electric Propulsion Conference, Wiesbaden, Germany, 2011.
- [10] Pottinger, S., Lappas, V., Charles, C., and Boswell, R. “Performance Characterization of a Helicon Double Layer Thruster Using Direct Thrust Measurements.” *Journal of Physics D: Applied Physics*, Vol. 44, No. 23, 2011, p. 235201. <https://doi.org/10.1088/0022-3727/44/23/235201>.
- [11] ANU News » Revolutionary Thruster Set for Space Launch. <https://web.archive.org/web/20090602054431/http://news.anu.edu.au/?p=1148>. Accessed Sep. 19, 2022.
- [12] Slough, J., Kirtley, D., and Weber, T. Pulsed Plasmoid Propulsion: The ELF Thruster. Presented at the 31st International Electric Propulsion Conference, Ann Arbor, Michigan, U.S.A., 2009.
- [13] Furukawa, T., Takizawa, K., Kuwahara, D., and Shinohara, S. “Study on Electromagnetic Plasma Propulsion Using Rotating Magnetic Field Acceleration Scheme.” *Physics of Plasmas*, Vol. 24, 2017. <https://doi.org/10.1063/1.4979677>.

- [14] Furukawa, T., Kuwahara, D., and Shinohara, S. “Spatial Characteristics of Rotating Magnetic Field (RMF) Plasma Acceleration Method in Open Magnetic Field Configuration under Partial RMF Penetration.” *Physics of Plasmas*, Vol. 28, No. 7, 2021, p. 073507. <https://doi.org/10.1063/5.0035383>.
- [15] Shinohara, S., Kuwahara, D., Ishigami, Y., Horita, H., and Nakanishi, S. “Extremely Small-Diameter, High-Density, Radio Frequency, Plasma Sources and Central Gas Feeding for next-Generation Electrodeless Plasma Thrusters.” *Review of Scientific Instruments*, Vol. 91, No. 7, 2020, p. 073507. <https://doi.org/10.1063/5.0003387>.
- [16] Siddiqui, U., and Cretel, C. “Updated Performance Measurements and Analysis of the Phase Four RF Thruster.” *2018 Joint Propulsion Conference*, American Institute of Aeronautics and Astronautics.
- [17] Yost, B., Weston, S., Benavides, G., Krage, F., Hines, J., Mauro, S., Etchey, S., O’Neill, K., and Braun, B. “State-of-the-Art Small Spacecraft Technology.” NASA TP 20210021263. 2021.
- [18] REGULUS Datasheet. https://www.t4innovation.com/wp-content/uploads/2019/10/T4i_REGULUS_datasheet_.pdf. Accessed Sep. 19, 2022.
- [19] Levchenko, I., Xu, S., Mazouffre, S., Lev, D., Pedrini, D., Goebel, D., Garrigues, L., Taccogna, F., and Bazaka, K. “Perspectives, Frontiers, and New Horizons for Plasma-Based Space Electric Propulsion.” *Physics of Plasmas*, Vol. 27, No. 2, 2020, p. 020601. <https://doi.org/10.1063/1.5109141>.
- [20] Hugrass, W. N., Jones, I. R., McKenna, K. F., Phillips, M. G. R., Storer, R. G., and Tuzek, H. “Compact Torus Configuration Generated by a Rotating Magnetic Field: The Rotamak.” *Physical Review Letters*, Vol. 44, No. 25, 1980, pp. 1676–1679. <https://doi.org/10.1103/PhysRevLett.44.1676>.
- [21] Milroy, R. D. “A Numerical Study of Rotating Magnetic Fields as a Current Drive for Field Reversed Configurations.” *Physics of Plasmas*, Vol. 6, No. 7, 1999, pp. 2771–2780. <https://doi.org/10.1063/1.873234>.
- [22] Milroy, R. D. “A Magnetohydrodynamic Model of Rotating Magnetic Field Current Drive in a Field-Reversed Configuration.” *Physics of Plasmas*, Vol. 7, No. 10, 2000, pp. 4135–4142. <https://doi.org/10.1063/1.1290279>.
- [23] Brunkhorst, C., Berlinger, B., Ferraro, N., and Cohen, S. A. The Princeton FRC Rotating-Magnetic-Field-Experiment RF System. Presented at the 2007 IEEE 22nd Symposium on Fusion Engineering, 2007.
- [24] XR2206 Datasheet. <https://www.jameco.com/Jameco/Products/ProdDS/34972.pdf>. Accessed Feb. 23, 2023.
- [25] Oliveira, L. B., Fernandes, J. R., Filanovsky, I. M., Verhoeven, C. J. M., and Silva, M. M. “Transceiver Architectures and RF Blocks.” *Analysis and Design of Quadrature Oscillators* (L. B. Oliveira, J. R. Fernandes, I. M. Filanovsky, C. J. M. Verhoeven, and M. M. Silva, eds.), Springer Netherlands, Dordrecht, 2008, pp. 7–35.
- [26] LT1210 Datasheet. <https://www.analog.com/media/en/technical-documentation/data-sheets/lt1210.pdf>. Accessed Mar. 24, 2023.
- [27] SS49E Datasheet. <https://prod-edam.honeywell.com/content/dam/honeywell-edam/sps/siot/en-us/products/sensors/magnetic-sensors/linear-and-angle-sensors/common/documents/sps-siot-ss39et-ss49e-ss59et-product-sheet-005850-3-en-ciid-50359.pdf?download=false>. Accessed Apr. 14, 2023.

Appendix A – Derivation of Reactance Testing Equation

Consider the circuit in Figure 4.8. Consider that the source voltage in the time domain is given by Eq. (A.1).

$$v_S(t) = A_S \cos(\omega t + \theta_S) \quad (\text{A.1})$$

The voltage across the resistor in the time domain is given by Eq. (A.2).

$$v_R(t) = A_R \cos(\omega t + \theta_R) \quad (\text{A.2})$$

In the complex phasor domain, these voltages can be represented by Eqs. (A.3) and (A.4).

$$\tilde{V}_S = A_S e^{j\theta_S} \quad (\text{A.3})$$

$$\tilde{V}_R = A_R e^{j\theta_R} \quad (\text{A.4})$$

In the phasor domain, the voltage across the resistor is also given by Eq. (A.5).

$$\tilde{V}_R = \tilde{I} Z_R \quad (\text{A.5})$$

The circuit is entirely in series, so the current phasor is given by Eq. (A.6).

$$\tilde{I} = \frac{\tilde{V}_S}{Z_L + Z_R} \quad (\text{A.6})$$

Combining Eqs. (A.5) and (A.6) gives Eq. (A.7).

$$\tilde{V}_R = \frac{Z_R \tilde{V}_S}{Z_L + Z_R} \quad (\text{A.7})$$

Rearranging Eq. (A.7) gives Eq. (A.8).

$$\frac{\tilde{V}_R}{\tilde{V}_S} = \frac{Z_R}{Z_L + Z_R} \quad (\text{A.8})$$

As shown in Figure 4.8, the impedance of the resistor and inductor are given by Eqs. (A.9) and (A.10).

$$Z_R = R \quad (\text{A.9})$$

$$Z_L = R_L + jX_L \quad (\text{A.10})$$

Substituting these values into Eq. (A.8) gives Eq. (A.11).

$$\frac{\tilde{V}_R}{\tilde{V}_S} = \frac{R}{R_L + jX_L + R} \quad (\text{A.11})$$

Since both sides of Eq. (A.11) are complex numbers that are equal, their magnitudes must also be equal. Equating the magnitudes of both sides of Eq. (A.11) gives Eq. (A.12).

$$\left| \frac{\tilde{V}_R}{\tilde{V}_S} \right| = \left| \frac{R}{R_L + jX_L + R} \right| \quad (\text{A.12})$$

An expression for the right-hand side of Eq. (A.12) can be found through the process shown in Eq. (A.13).

$$\left| \frac{R}{R_L + jX_L + R} \right| = \frac{|R|}{|R_L + jX_L + R|} = \frac{R}{\sqrt{(R + R_L)^2 + X_L^2}} \quad (\text{A.13})$$

An expression for the left-hand side of Eq. (A.12) can be found through the process shown in Eq. (A.14).

$$\left| \frac{\tilde{V}_R}{\tilde{V}_S} \right| = \frac{|\tilde{V}_R|}{|\tilde{V}_S|} = \frac{A_R}{A_S} \quad (\text{A.14})$$

Since the test conditions described in Section 4.3 are set up such that the amplitude of the voltage across the resistor is half of the amplitude of the source voltage, the assertion of Eq. (A.15) can be made.

$$\frac{A_R}{A_S} = \frac{1}{2} \quad (\text{A.15})$$

Substituting Eqs. (A.13) and (A.15) into Eq. (A.12) gives Eq. (A.16).

$$\frac{R}{\sqrt{(R + R_L)^2 + X_L^2}} = \frac{1}{2} \quad (\text{A.16})$$

Solving Eq. (A.16) for X_L gives Eq. (A.17).

$$X_L = \pm \sqrt{3R^2 - 2R_L R - R_L^2} \quad (\text{A.17})$$

Inductors have positive reactance, so the positive solution of Eq. (A.17) is taken. This gives Eq. (A.18), which is the equation used in Section 4.3.

$$X_L = \sqrt{3R^2 - 2R_L R - R_L^2} \quad (\text{A.18})$$

It should be noted that this analysis has assumed that the inductor is not ideal, i.e. that it has some non-zero DC resistance. For an ideal inductor, R_L is zero, and Eq. (A.18) reduces to Eq. (A.19).

$$X_L = \sqrt{3}R \quad (\text{A.19})$$

Since the reactance tests performed in Chapter 4 included the DC resistance of the coils, Eq. (A.18) was used.